Experimental and numerical analysis on the shear capacity of demountable connections for prefabricated 3DCP elements

Driessen, Saar A.

Award date:
2023

EINDHOVEN UNIVERSITY OF TECHNOLOGY

Faculty Architecture Building and Planning
Unit Structural Engineering and Design

Experimental and numerical analysis on the shear capacity of demountable connections for prefabricated 3DCP elements.

Master's Thesis

S.A. (Saar) Driessen

Supervisors:
Prof. Dr. Ir. A.S.J. (Akke) Suiker
Dr. Ir. R.J.M. (Rob) Wolfs
Ir. D.H. (Derk) Bos

Eindhoven, July 2023

Preface

Six years ago, I decided to start the bachelor Architecture, Urbanism and Building Sciences due to its combination of design and technical courses. Six years later, about to finish my master's degree Structural Engineering and Design, I am still very grateful for that decision, and I was more than happy to be able to have a bit of both aspects in my graduation project about demountable connections in 3D concrete printed elements as well. While my research project started with a lot of brainstorming and designing, it ended with detailed analyses of the behaviour of sinusoid connections, being a perfect combination for me.

Of course, I could not have done this research alone. First of all, I would like to thank Rob Wolfs for his guidance and all our interesting discussions along the way. Our meetings kept me critical and were always valuable. Furthermore, I would like to thank Akke Suiker for sharing his knowledge and guiding me through the numerical parts of my research. I wanted to include applied mechanics in my research, and thanks to you, I was able to do that. I also want to thank Derk Bos for completing my graduation committee.

Besides my numerical parts, a large part of my research was experimental. For this, I spent much time in the structural design laboratory at the Technical University of Eindhoven. I would like to thank all the laboratory employees, especially Hans Lamers and Theo van Loo, for their guidance, enthusiasm and entertainment during my time there. Furthermore, I would like to thank Matthew Ferguson for his guidance with the robots. Without him, I would not be able to actually print some specimens, which (in the end...) was very rewarding. Thank you for being so patient during all the failed attempts, and I hope it will only go better from now on.

I would also like to thank Ralf Eemers (and his computer) for all the emotional support and extra computational power. Lastly, I would like to thank my family, friends and fellow students for their support and love during the last year and during my studies as a whole. Because of you, I always had a great time!

Abstract

The development of additive manufacturing, and 3D concrete printing (3DCP) specifically, can solve the two significant challenges the construction industry faces today by using digital manufacturing and prefabrication to increase productivity and optimising material usage and reducing waste to decrease the environmental impact. Furthermore, the industry can shift from a linear economy model towards a circular model by using demountable connections between the prefabricated elements. Therefore, this research aims to establish design recommendations for demountable connections in prefabricated 3DCP elements. Previous research on traditional precast connections has shown that demountable connections often have two attention points: extreme loading conditions could lead to sudden disassembly, and high stress concentrations could arise at the points of attachment. However, recent research on dry connections did show promising results with shear or bending capacities almost equal to the capacities of monolithic elements.

To establish design recommendations, first, a preliminary analysis was performed to determine a promising geometry. It was found that a sinusoid geometry has a lot of potential because the round shapes reduce stress concentrations and make the manufacturing process more simple. Furthermore, this geometry has two different failure mechanisms (sliding along the sinusoid interface or fracture), making it adaptable to varying sets of requirements. A more detailed experimental and finite element analysis on the shear capacity and the failure response was performed for a sinusoid connection to determine the influence of the wavelength, amplitude, prestressing force and roughness. For the experimental analysis, a double shear push-out test was performed for different geometries and prestressing forces. This test set-up was also modelled in a finite element analysis. Cohesive zones were included to model fracture.

This analysis showed that if the required shear capacity is small, it is recommended to use a small maximum angle to design a connection that fails due to sliding, as this failure mechanism has a large deformation capacity and designing a smaller angle could simplify the manufacturing process. The shear capacity for this failure mechanism can be increased by increasing the maximum angle (increase amplitude or decrease wavelength) of the sinusoid geometry, the prestressing force or the friction coefficient. If a high shear capacity is required, a connection which fails due to fracture should be designed, as high shear forces cannot be achieved without a fracture failure mechanism. For this failure mechanism, the shear capacity can be increased by decreasing the amplitude, increasing the wavelength and increasing the prestressing force. Depending on the amount of prestress, a connection with a mode I (large amplitude) or mode II (small wavelength) failure mechanism can be designed.

These conclusions are verified in a case study for which a small-scale shear wall is designed. The wall is subjected to a shear force, and the shear capacity is compared to a monolithic version of the wall. The results show that the ultimate shear force of the designed connections is similar to the design force and that the tested wall consisting of four parts connected with sinusoid connections has a shear capacity of 83.12% and a higher deformation capacity compared to a monolithic wall. It can therefore be concluded that the sinusoid connection shows a lot of potential, although some further research is required to develop a calculation method and use the connection in practice.

Contents

List of Figures

List of Tables

List of Symbols

α	Maximum angle of a sinusoid geometry	deg
β	Mode mixity parameter	-
ϵ	Factor to prevent damge to be completed	-
η	Relaxation parameter	s
κ	Deformation history parameter	mm
λ	Wavelength	mm
μ	Coefficient of friction	-
τ	Shear stress	MPa
σ_b	Bending stress	MPa
σ_{cp}	Axial stress due to applied prestress	MPa
A	Amplitude	mm
D_{max}	Maximum aggregate size	mm
E_c	Young's modulus	MPa
F	Ultimate shear force	kN
$G_{I,c}$	Fracture toughness mode I	N/mm
$G_{II,c}$	Fracture toughness mode II	N/mm
K	Elastic stiffness cohesive elements	MPa
P	Prestressing force	kN
P_a	Average roughness	mm
R_z	Roughness parameter: mean peak-to-vally height	mm
d	Damage parameter	-
f_t	Tension strength	MPa
h	Heigth of the specimen	mm
t_1^u	Ultimate traction mode I	MPa
t_2^u	Ultimate traction mode II	MPa
t_i	Traction	MPa
ν_c	Poisson's ratio	-
ν_i	Relative displacement across the interface	mm
ν_{sh}	Total shear displacement ($\sqrt{\nu_2^2 + \nu_3^2}$)	mm

Chapter 1

Introduction

1.1 Problem definition

The development of Additive Manufacturing (AM) within the construction industry can solve the two significant challenges the construction industry faces today: a high environmental impact and a relatively low productivity. The construction industry is responsible for almost 40% of the carbon emissions and around 30 % of the consumption of natural resources [4]. Furthermore, due to a linear economy model, meaning "take, make, dispose of" [9], the construction industry is responsible for 25% of the waste worldwide. By using AM methods, material usage and generation of waste can be reduced. To reduce the amount of waste and the consumption of natural resources even more, the construction industry has to shift from that linear economy model towards a circular economy model, where "the aim is to keep products, components, and materials at their highest utility and value at all times" [9].

Furthermore, there is a high demand to increase productivity, resulting in more prefabrication within the construction industry. For 3D concrete printing (3DCP), one of the AM methods, most printing is done off-site in a controlled environment, as humidity and temperature significantly influence the material strength [19]. If these prefabricated concrete printed elements would be connected with a demountable connection, the whole structure could be disassembled and reused in some form without reducing the value of the elements, which leads to not only a higher productivity due to prefabrication and additive manufacturing but also a circular economy. Therefore, this research focuses on exploring and designing demountable connections between prefabricated 3DCP elements. Different shapes and the effect of varying different parameters within a certain shape will be analysed to get an understanding of the possibilities of demountable connections.

1.2 Research objective

The research goal for this graduation project can be summarised by the following objective:

> *Establish design recommendations for demountable connections in prefabricated 3D concrete printed elements based on the varying shear capacity.*

The research objective is divided into the following sub-questions:

- What types of connections are possible given the manufacturability, the required force transmissions and the properties of 3DCP?
- How do the following parameters influence the mechanical behaviour and the manufacturability of the connection?
  - Varying the type of geometry
  - Varying different geometry parameters within one geometry type
- How does a dry connection perform compared to a monolithic element?

1.3 Methodology

To establish design recommendations as stated in the research goal, first, a preliminary analysis was performed to answer the first sub-question. This analysis was performed numerically and experimentally and aimed to find the influence of different geometry types on mechanical behaviour, manufacturability, and adaptability and which geometry type had the most potential. The most promising geometry type was used for a more detailed study of the effect of varying different parameters on the mechanical behaviour and manufacturability. This detailed study consists of an experimental analysis, a numerical finite element analysis, and two analytical approaches. These results were used to establish design recommendations for the shear capacity of a demountable connection. To verify these recommendations and to answer the last sub-question, a case study was performed in which a shear wall consisting of four elements connected by demountable connections was compared to a monolithic shear wall. The connections were designed for a certain shear force according to the set recommendations, and the resulting ultimate shear forces were compared to the design forces.

1.4 Thesis outline

This thesis provides insight into the possibilities and the behaviour of demountable connections between prefabricated 3D concrete printed elements. Chapter 2 describes the theory of connections in prefabrication, the state of the art of dry connections and the manufacturing methods. Chapter 3 describes the preliminary study performed to analyse different possible geometries and their potential. Afterwards, a more detailed experimental and numerical analysis was performed on a sinusoid connection, as described in chapters 4 until 6. Based on the production of the specimens for the experimental analysis, some findings on manufacturability are presented in chapter 7. The results of the experimental and numerical analysis were verified in a case study, described in chapter 8, after which the conclusions and recommendations can be found in chapter 9.

Chapter 2

Theory

2.1 Traditional precast connections

In prefabrication, connections have to make a coherent structure from all separate elements, which is able to absorb all forces present. Therefore, the performance of the connections is the most important consideration in precast concrete structures [10]. A connection should be strong enough to transfer all forces applied to it during its lifetime. Furthermore, it should not restrict deformations of the structure itself. For example, a beam always has some deformation, the connection should have enough deformation capacity to deform along with the beam. Lastly, ductility should be kept in mind. It is preferable that brittle failure is prevented and that a connection has some ductile behaviour. [11]

According to Messler [21], there are two general rules when designing a connection: One should select a joining process that minimises the changes or disruptions to the material's microstructure, and one should keep in mind the effects of the created connection on the final structure. Messler states that "It is fairly safe to say that fewer parts, simpler shapes, and less-sophisticated, lower performance materials require less elaborate joining processes and procedures." Therefore, the simplicity of the connections should be considered.

There are three fundamental joining methods: mechanical joining, adhesive bonding and welding. Of these three methods, mechanical joining often allows for disassembly without damaging the involved parts. In conventional prefabricated structures, elements are often connected either by mechanical fasteners or by the well-known Corbel connection. Both connections make use of the mechanical joining method [29][3]. However, there are two significant drawbacks to these connections: (i) under extreme loading conditions, accidental disassembly could occur without any precautions, and (ii) often stress concentrations are introduced at points of fastening or attachment [21]. For example, when looking at the Corbel connection, a dowel is often cast into the corbel to prevent sudden disassembly [23]. However, adding this dowel combines the mechanical joining method with the adhesive bond method, making it difficult to disassemble the connection. These two attention points, as well as keeping the connection as simple as possible, should be considered when designing new connections.

2.2 Recent research to dry connections

Due to the risk of sudden disassembly, dry connections are not often used in the current construction industry. However, history shows that dry connections have a lot of potential. For example, the old Japanese architecture shows temples, shrines and three- to five-story pagodas, all constructed with traditional Japanese joinery, being dry joints constructed out of timber [30]. As the popularity of prefabrication is rising, more research is being done towards dry connections. At first, mostly in the timber industry. For example, researchers showed that a scarf timber joint loaded in bending has a stiffness of 70-92% compared to a solid beam, and the strength is around 55% compared to a solid beam [16].

But besides timber joints, due to the developments of CNC-controlled production within the concrete industry, a lot of research is being done to dry concrete connections as well [20]. Lehmberg et al. looked into the potential of toothed strips as dry joint connections for plate elements. They tested the connection under various bending and in-plane shear loading and found promising results. For certain geometries, it was even possible to have a higher load-bearing capacity than the monolithic reference plate [18]. Furthermore, Bagdadi et al. did research to dry beam-to-beam connections [2] and dry joints in 3D concrete printed portal frames [3]. For the beam-to-beam connection, they found that certain geometries reached 85% of the full beam bending capacity. For the joints in portal frames, Baghdadi et al. tested eight different geometries for which the bending capacity was between 50% and 106% compared to the monolithic elements and the initial stiffness was between 51% and 124%. For this research, the robotic manufacturability of the connections was analysed as well, making use of the shotcrete printing method and milling. These researches prove the potential of dry connections but also show that the geometry of the connection is of high importance as the performance can vary a lot.

2.3 Robotic manufacturing

2.3.1 3D concrete printing

This research is about connecting elements made with 3D concrete printing (3DCP). This technique is a digital fabrication method for cementitious materials. Different 3D printing technologies can be used for concrete printing, this research is based on a layered extrusion method. In this method, a digital model is sliced into 2-dimensional layers. Subsequently, a nozzle precisely extrudes the material in the shape of these layers, and the final object is created layer by layer.

For this manufacturing method, no formwork is used. However, the formwork usually stabilises the fresh concrete until it is sufficiently hardened. Due to the lack of formwork, the concrete should have a certain stiffness immediately after extrusion to remain in its correct shape. But before extrusion, the material must be workable enough to be transported through the whole system (pump, hose and nozzle). Therefore, Portland cement is usually used where an additive is added to enhance the setting rate. To ensure the material is workable enough, the aggregate size is often limited to around a maximum of 1 millimetre.

As mentioned, 3DCP can reduce the amount of labour. Furthermore, as no formwork is needed, less waste is generated. The material used for formwork in the concrete construction can be more than half of the total material used [15], so removing the formwork reduces the environmental footprint significantly. Another advantage of 3DCP is that due to the digitised process and the lack of formwork, there is a high design freedom. This can have an architectural benefit, but it can also optimise the structural performance of an element.

2.3.2 Subtractive manufacturing

As mentioned, 3DCP gives a lot of design freedom, which makes it possible to manufacture more complex connections compared to traditional casting of concrete. However, when higher precision is required, subtractive shaping processes are more suitable compared to additive shaping processes like 3DCP [8]. Therefore, it could be beneficial to use a subtractive shaping process in combination with the additive shaping process to gain a higher precision. A subtractive shaping method which is easy to apply on concrete (when performed in the green state) is milling. And as the SED laboratory at the Technical University of Eindhoven has the required tools for milling, this is the most logical method to use for this research.

The time window in which the milling happens is critical for the result, as the state of the concrete significantly influences the surface quality after milling. Dobrzanski et al. [8] tested the influence of the concrete state on the milling process. The setting range of the concrete was determined with a Vicat test, and specimens in different states were tested. It was found that by milling concrete in the plastic state, a flat surface with an average roughness (P_a) equal to 0.25mm could be produced

(concrete cast against a steel mould results in a roughness of 0.015mm). When the concrete hardens more, the roughness decreases, and the results improve. However, the tools required to mill have to be much stronger. The robotic arms commonly used for 3DCP are not strong enough to mill concrete in a plastic-solid or solid state. Ferguson [12] came to the same results. This research showed that for the Weber3D 145-2 concrete mix, the best results were achieved at a material age of 1.5-2.5 hours.

Furthermore, the aggregate size influences the surface quality. Especially in the plastic state of concrete, the matrix is not strong enough to hold the aggregates in place. Therefore, they will be pulled out or displaced through the matrix instead of going through the aggregates, leading to a lower surface quality. The larger the aggregates are, the larger the effects of the pull-out and displacement mechanisms are. [8]

Chapter 3

Preliminary study

3.1 Introduction

After studying existing connections and their potential, as used for concrete, but also for other materials like timber, three categories of geometries were classified. These geometries were used as a starting point for this research and are visualised in figure 3.1. A numerical and experimental preliminary study was performed to study the potential of these different geometries. The connections were evaluated on their structural behaviour, manufacturability and adaptability.

(a) Lego connection

(b) sinusoid shape [14]

(c) Dapped-end [24]

Figure 3.1: Three possible categories of geometries for a dry connection

3.2 Numerical analysis

To be able to compare the three different geometry types given in figure 3.1, first, a numerical analysis was performed on a wide variety of geometries belonging to one of the three categories. This analysis aimed to get an understanding of the influence of certain shape parameters and to find promising configurations for the three different geometries. The promising configurations were used in the experimental analysis presented in section 3.3.

3.2.1 Methodology

A numerical analysis of a double shear push-out test was performed to analyse the shear capacity of the different geometries. 2D linear elastic analyses were performed in Abaqus. As a double shear push-out test is symmetrical, only half of the test is modelled, the geometry and boundary conditions of the analyses are visualised in figure 3.2. The geometries were designed in grasshopper and Rhino. These geometries were exported as an ASIC file, which can be imported into Abaqus as a sketch. For each analysis, first the prestress is applied as a surface pressure force, after which the shear force is applied as a vertical deformation. Contact between the different parts was defined as surface-to-surface contact, for which hard contact was defined as normal behaviour and friction was defined as tangential behaviour using the penalty method. This type of contact definition was also used in a similar study to dry connections performed by Baghdadi et al. [3]. For the linear friction coefficient a value of 0.4 was

applied [22]. 4 node plane stress quadrilateral mesh elements (CPS4R) were used and the average number of elements in the left and right part is equal to 6200 and 4200 elements, respectively. The mesh density is increased closer to the interface. At the interface, a mesh size of 1.0mm is used, while the largest mesh size within the analysis equals 5.0mm.

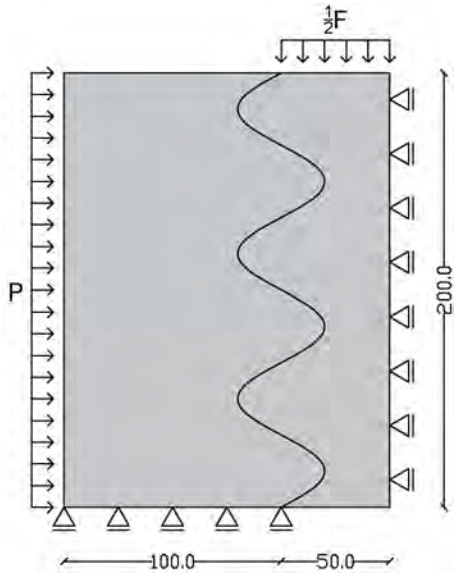

Figure 3.2: Geometry, boundary conditions and dimensions (in millimetres) of the numerical analysis

3.2.2 Results

This section describes the observations made during the numerical analysis per geometry type. A straight interface has an ultimate shear force of the friction coefficient multiplied by the prestressing force, thus $F = 0.4 \cdot 100$ N/mm= 40 N/mm. This value represents the force per millimetre depth as the analyses were performed in 2D. In the next paragraphs, the different geometries are compared to this resistance. Furthermore, the influence of adjusting different geometrical parameters is presented for each type of geometry.

LEGO connection

Adding a notch increases the maximum shear force significantly compared to a straight surface. Instead of sliding out, the force keeps increasing until the simultaneously increasing stresses result in fracture, although fracture properties are not modelled in this analysis. If no frictional behaviour is included in the model, a slip-out behaviour can be seen, although both tensile and compressive stresses would have long exceeded their limit if fracture was included. This slip-out force and the magnitude of the stresses keep the same if friction on only the vertical surfaces is included. This indicates that the friction of those surfaces does not add to the performance of the connection. However, when friction is included on the top surface of the notch, the shear force keeps increasing and is significantly higher than before. Furthermore, it was observed that the smaller the angle of the top surface of a notch, the larger the shear force.

Table 3.1 indicates the shear force at a vertical displacement of 0.5mm and at a maximum tensile stress of 4MPa. The latter value represents the moment of fracture. The magnitude of 4MPa is an assumption, but as the relationship between the increase of force and the increase of stress within the analyses was linear, the relations visible in table 3.1 are prone to be realistic. In the table, it can be seen that the ultimate shear force and the stiffness both increase when more notches are added to the connection. However, this effect becomes smaller with an increasing number of notches, and at four notches it even reveres. When the notches' depth increases, the shear force also increases. However,

at some point, the thickness of the notch reaches an optimum, as after that, not the whole notch is loaded. Increasing the height of the notches mostly influences the maximum stresses and, therefore, the shear force at a maximum tensile stress of 4MPa, as indicated in table 3.1. When looking at the shear stresses, as plotted in figure 3.3, it can be concluded that when the height of a notch is larger, the shear forces can be divided along a larger surface, resulting in smaller shear stresses. This effect is mostly visible in the first notch. It seems that a larger height of the notch on the supporting part (left) is more important than on the loaded part (right), as the geometry with a large notch height (c) performs better than the geometry with an intermediate height (b).

Table 3.1: Effect on stiffness and ultimate force for varying LEGO geometries

Number of notches	**1**	**2**	**3**	**4**
Force at u2=0.5mm [N/mm]	4100	8300	10600	12300
Force at σ_{max}=4MPa [N/mm]	55	85	145	130
Depth of the notches	**5mm**	**10mm**	**15mm**	**20mm**
Force at u2=0.5mm [N/mm]	9100	10600	11200	11300
Force at σ_{max}=4MPa [N/mm]	119	145	160	125
Height of the notches	**20mm**	**30mm**	**40mm**	
Force at u2=0.5mm [N/mm]	5200	5500	5600	
Force at σ_{max}=4MPa [N/mm]	100	120	150	

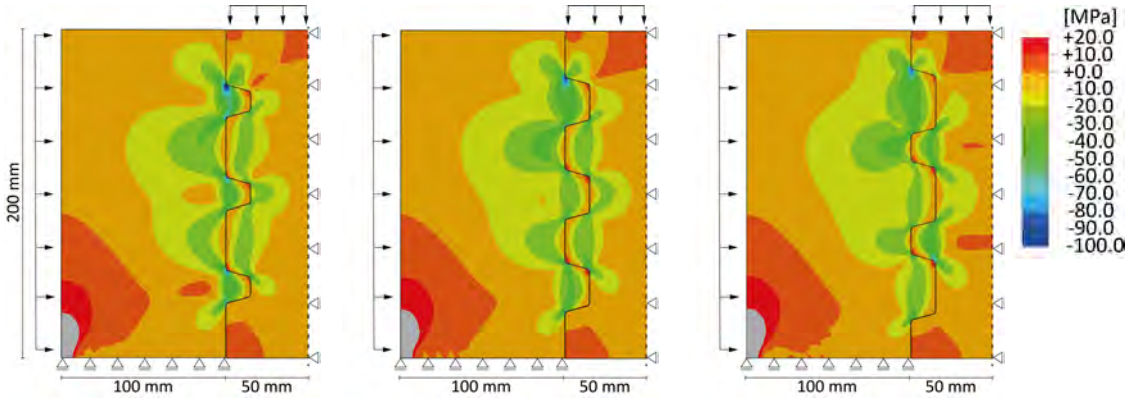

(a) Small height **(b)** Intermediate height **(c)** Large height

Figure 3.3: Shear stresses (S12) within a LEGO-shaped connection for varying heights of the notches

Sinusoid connection

Adding a sine wave to the interface results in an ultimate shear force being around three times higher compared to a straight interface. The stresses also increase, but for a small sine wave, they are still in a range where no fracture will occur. When no frictional properties are included in the model, the shear force drops significantly, meaning that the Coulomb frictional behaviour has a significant contribution to the ultimate shear force in this connection.

When looking at the effect of the wavelength on the behaviour of the connection, table 3.2 shows that the smaller the wavelength, the higher the slip-out force is. This correlation seems to be exponential; the smaller the wavelength, the larger the force increase. Simultaneously with the force increase, the stresses increase. Therefore, the failure mechanism changes from slipping out to fracture at some point. The same effects can be seen when varying the amplitude. Again an exponential relation seems to exist between an increase in amplitude and an increase in slip force. When varying the wavelength, the start position should be considered carefully. If the sine wave of the supporting block starts going outwards, high stress concentrations arise at the top of the connection, as can be seen in figure 3.4.

Table 3.2: Effect on stiffness and ultimate force for varying sinusoid geometries

	Wave length			**Amplitude**			
	1h	1/2h	1/3h	10mm	15mm	20mm	25mm
Force at plateau [N/mm]	107	214	409	137	214	328	511
Force at σ_{max} ≤4MPa [N/mm]	107	202	228	137	202	235	231

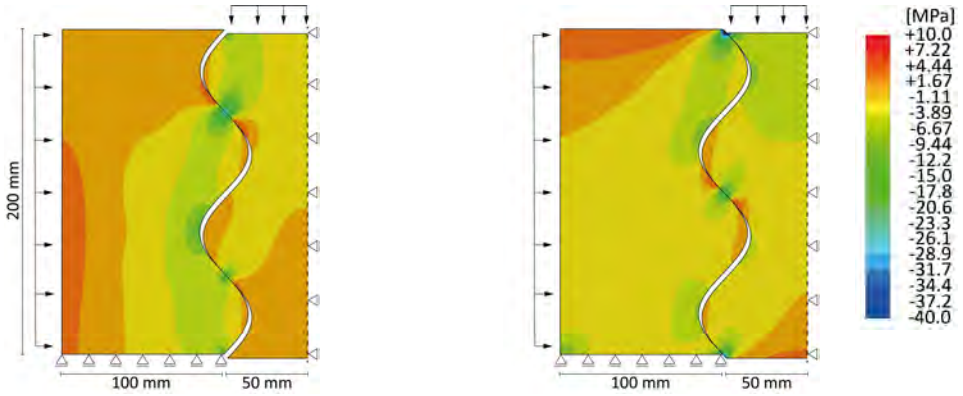

(a) Sine wave of supporting block starting inwards **(b)** Sine wave of supporting block starting outwards

Figure 3.4: Maximum principle stresses showing high stress concentrations when the start position of the sine wave is not considered carefully

Dapped-End connection

Adding a notch, i.e., creating a traditional dapped-end beam connection, significantly increases the maximum shear force compared to a straight surface. The behaviour is similar to the Lego shape; instead of sliding out, the force keeps increasing until the simultaneously increasing stresses result in fracture. Excluding friction in the model does not influence the behaviour significantly. Therefore, the Coulomb frictional behaviour does not seem to play an essential role in this type of connection.

When varying the depth of the notch, table 3.3 shows that the resistance of the connection increases when the depth of the notch increases. When the depth is too small, around 10 millimetres, the area to transfer forces is also small, leading to significantly higher principle stresses (both compressive and tensile stresses). Therefore, increasing the depth leads to a higher force at fracture. However, when the depth becomes even larger (25mm), table 3.3 shows that the force at fracture decreases again. The larger lever arm seems to have a significant role in this case. The total depth of the notch could also be split into two steps, creating the shape of a stair. This results in a higher force at fracture, the force can be transferred at two locations and therefore the stresses are better divided.

Table 3.3: Effect on stiffness and ultimate force for varying Dapped-end geometries

	Depth of the notch					
	10mm	15mm	20mm	25mm	30mm	2x 12.5mm
Force at u2=0.5mm [N/mm]	2100	2350	2550	2700	2800	3200
Force at σ_{max}=4MPa [N/mm]	98	107	124	137	130	152

Comparison

All three shapes showed a significant increase in shear resistance compared to a straight interface. For the sinusoid geometry, Coulomb frictional behaviour significantly influenced the ultimate shear force, whereas, for the other two geometries, the interlocking effect was considerably higher than the contribution of frictional behaviour. The stress distribution of all three geometry types is illustrated in figure 3.5 by plotting the maximum principle stress. The stress distribution indicates high stress concentrations at the sharp corners of the Lego geometry (3.5a) and the dapped-end geometry (3.5c).

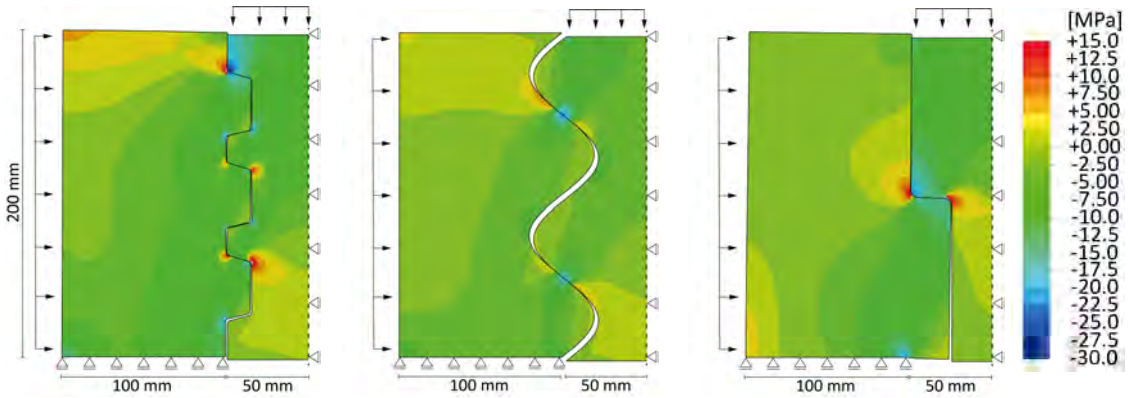

(a) **(b)** **(c)**

Figure 3.5: Maximum principle stresses of the Lego geometry (a), sinusoid geometry (b), and the dapped-end geometry (c)

3.3 Experimental analysis

3.3.1 Methodology

Based on the results of the numeric analysis, three variants were determined for each geometry category. These geometries were used for a double-shear push-out test to analyse the mechanical performance of the three different geometry types. This experimental analysis aimed to establish which of the three geometry types is most promising. The properties of the variants are given in table 3.4. An interlayer was included for one variant of each category to distribute the stresses and prevent high stress concentrations. Granulated rubber was used as an interlayer with a thickness of 2 millimetres. An interlayer was added to avoid a scenario where all specimens fail due to high stress concentrations at the interface. The dimensions of the specimen were set to 200x100x100mm. These dimensions were chosen because it is large enough to minimise the influence of individual aggregates ($D_{max} = 1mm$). These dimensions are comparable to those used in the research of Bischof et al. [5].

Table 3.4: Geometrical properties of specimens

Variant	Shape properties	Interlayer
Sine - variant 1	Wavelength (λ): 0.5h (100mm), amplitude: 20mm	No
Sine - variant 2	Wavelength (λ): 0.5h (100mm), amplitude: 20mm	Yes
Sine - variant 3	Wavelength (λ): h (200mm), amplitude: 20mm	No
Lego - variant 1	Nr. notches: 3, height notch: 40mm, depth notch: 15mm	No
Lego - variant 2	Nr. notches: 3, height notch: 40mm, depth notch: 15mm	Yes
Lego - variant 3	Nr. notches: 2, height notch: 50mm, depth notch: 15mm	No
Dapped - variant 1	Depth of 25mm in one step	No
Dapped - variant 2	Depth of 25mm in one step	Yes
Dapped - variant 3	Depth of 25mm in two steps	No

Preparation of the specimen

For this preliminary study, it was decided to use cast specimens to minimise manufacturing deficiencies, such as inaccuracies in geometries or cavities in the printed layers. Baghdadi et al. used cast specimens in their research as well for similar reasons [3]. To be able to make the specimens, formwork was created. Three specimens were needed for each variant to perform a double-shear push-out test. The shapes of the interfaces were cut out of Styrofoam. For the LEGO and the Dapped-End connections, this was done by hand. The sine shapes were manufactured robotically. To ensure easy removal of the foam when removing the formwork, the foam parts were covered with a layer of plastic wrap. The foam parts were placed in plywood boxes, as visible in figure 3.6a As this research is about 3D concrete printing, the specimens were made with a cement mix usually used for 3DCP. The mix used is Weber3D 145-2. To be able to cast all specimens at once, the concrete is mixed inside the mixer and pump used for the 3D concrete printer. The distance from the pump to the formwork was equal for all specimens, as can be seen in figure 3.6b. This distance resulted in a good division of the material over the formwork. After pouring, the specimens were covered with plastic, as can be seen in figure 3.6c. After 24 hours, the formwork was removed, and the specimens were placed underwater for the remaining hardening period, see figure 3.6d. Besides the specimens for the direct shear test, three mortar beams were poured. These beams will be used for 3-point bending and compression tests to determine basic material properties.

(a) Formwork used to cast specimen

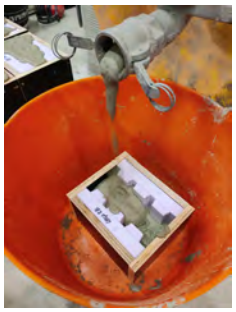

(b) Concrete being poured into formwork

(c) Hardening while covered for first 24 hours

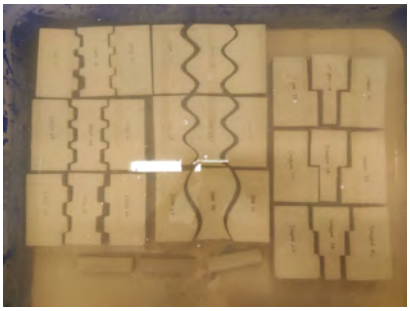

(d) Hardening while underwater for remaining time

Figure 3.6: Photos of the preparation of the specimen

Direct shear test

After 33 days, a double shear push-out test was performed. In figure 3.7 the test set-up can be seen. A hydraulic pump is installed on the right, applying a load-controlled prestressing force of 10kN on the specimens. This force was kept constant during the whole test. The set-up was placed in an Instron 250kN testing rig. This was used to apply a displacement-controlled loading at the top of the middle specimen. To ensure the load was uniformly distributed, a steel plate with a width of 90mm and a thickness of 30mm was placed between the Instron and the specimen. The deformation rate was set to 0.5mm/min. During the test, the deformation was measured in three places. Two LVDTs were placed at the bottom of the middle specimen on both sides, one of them is visible in figure 3.7. Furthermore, the Instron measures the displacement at the top. Besides the deformation, the rotation was measured on top of the left specimen.

After all variants had been tested, the third sine-shaped variant was tested again for different magnitudes of the prestressing force. The same specimens were used for these tests as no damage was visible. Each test was done with an identical deformation rate of 0.5mm/min, and the test was stopped as soon as a deformation of 0.2 millimetres was measured at the bottom LVDTs. After each test, the prestressing force was increased by 5kN. This was repeated until the prestressing force exceeded 40kN.

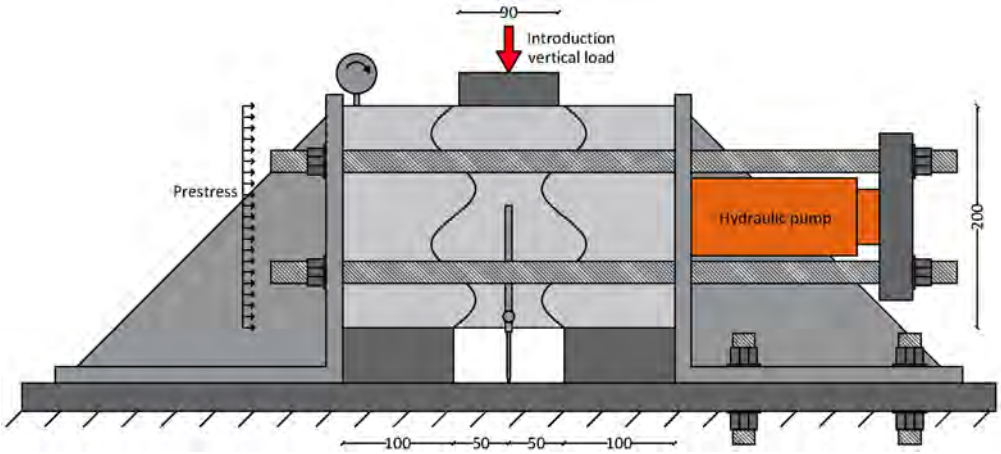

Figure 3.7: Test set-up double shear push-out test

Determination of flexural and compression strength

As a quality control and to compare the results with future tests, the flexural and compressive strength were determined according to the NEN 1015-11 [25]. During the preparation of the specimens, three additional specimens with dimensions of 160x40x40 were made. These three specimens were subjected to a load-controlled 3-point bending test. The load was applied at a uniform rate of 50 N/s. After the 3-point bending test, the two halves of each specimen were tested in a uni-axial compression test. This test was also load controlled, where the load was applied at a uniform rate of 2400 N/s.

3.3.2 Experimental results

The material properties of the specimens were determined with a 3-point bending test and a uni-axial compression test. The 3-point bending test showed an average flexural strength of 3.61 MPa with a relative standard deviation of 6.83%. The uni-axial compression test gave an average compressive strength of 43.03 MPa and a relative standard deviation of 7.74%. The results are slightly lower but comparable to values found in other research with a maximum deviation of 30% [1][13]. The relative standard deviations are not that high, but material deficiencies could cause small differences within the results of the direct shear tests.

In figure 3.8, the force-displacement response of all tested specimens can be seen. The vertical force applied to the middle specimen is plotted against the vertical deformation of this specimen. The displacement is determined by taking the average value of the two LVDTs at the bottom. The vertical deformation is measured after the prestressing force is applied. Applying the prestressing force could lead to some small deformations upwards (up to 0.3mm), but those deformations are not visible within the force-displacement responses in figure 3.8. As can be seen in the graphs, the maximum force found for each geometry is of a similar magnitude. Thus, the ability to transfer shear forces does not differ significantly between the different geometry types, although the defined shape parameters (e.g. notch depth, amplitude, etc.) have a considerably high influence on this ability. Most tested variants showed a sudden failure, as can be seen by the sharp peaks in the force-displacement responses. This sudden failure is not always acceptable, as a sudden collapse makes evacuating impossible.

The third variant with a sinusoid geometry was tested twice. This geometry did not fail due to fracture but started sliding, resulting in a slightly less sudden failure. To be able to slide downwards, the two outer blocks had to be pushed away, pushing against the prestressing force of 10kN. During the first run, the hydraulic pump used for the prestressing force had little room. Therefore, the test was stopped, more space was created, and it was performed again, resulting in the two curves (orange and green) visible in figure 3.8b. It can be seen that the peak visible in the first run is not visible anymore in the second run, but the plateau found afterwards is at the same force. This can be explained by the fact that inaccuracies in the interfaces of the specimens were smoothed out during the first run.

Some of the specimens were tested with an interlayer of granulated rubber. It was found that including this interlayer reduced the stiffness of the connections, as can be seen by comparing the blue (without) and orange (with) graphs in figures 3.8a and 3.8c. Furthermore, the peak force is lower for specimens with an interlayer. This may be caused by the fact that it was hard to get the interlayer in place, leaving some space between the specimens.

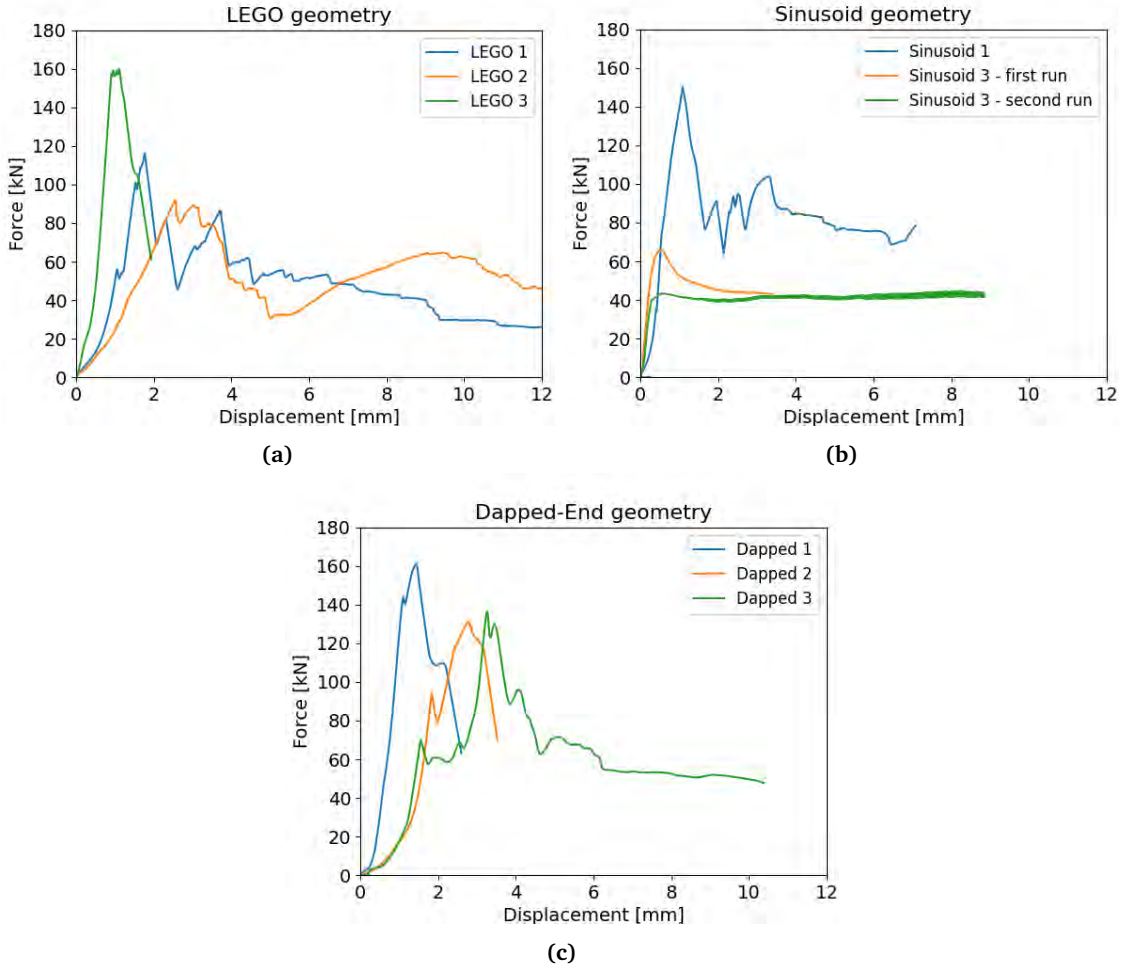

Figure 3.8: Force-displacement responses of the three geometry types. The second set of specimens for each geometry (visualized in orange) included an interlayer. Note that this set is missing for the sinusoid shape as this test failed and gave no results.

Effect of prestressing force on sliding resistance

The third variant with a sinusoid geometry, having a wavelength equal to the height of the specimen and an amplitude of 20 millimetres, was tested for different magnitudes of the applied prestressing force. The maximum force was determined for all tests and plotted in figure 3.9 (in blue). In this graph, it can be seen that the relationship between the prestressing force and the slip force is linear. The numerical model as presented in section 3.2.1 and visualized in figure 3.2 was calibrated to this data by adjusting the friction coefficient. The adjusted friction coefficient was defined as 0.63. The numerical results are also plotted in figure 3.9. The experimental and numerical results now show an identical relationship.

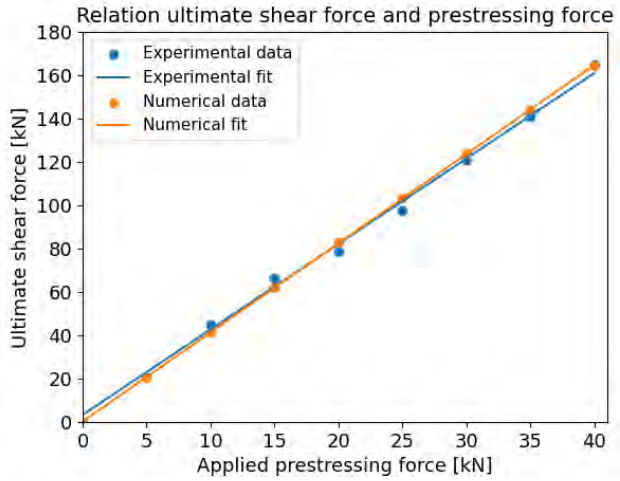

Figure 3.9: The experimental and numerical results of the ultimate shear force for sinusoid variant 3 plotted against the applied prestressing force, including a linear trend line.

In figure 3.10, the force-displacement curves are visible for different magnitudes of the prestressing force. Figure 3.10a shows the experimental results, and figure 3.10b shows the numerical results. Note that the scale of the x-axis differs for the experimental and numerical results. In both figures, it can be seen that the higher the prestressing force, the smoother the transition of the slope of the curve. For a low prestressing force, as soon as the end of the linear part of the force-displacement curve is reached, the force-displacement response makes a sharp transition toward a constant plateau. But if the prestressing force is higher, a smooth transition is visible after the linear part. This effect is visible in the experimental and the numerical results, although the transition zones are not the same magnitude. The differences in stiffness can be explained because the interfaces join perfectly into each other in the numerical analysis, while there were some deficiencies within the experimental analysis leading to more room to displace.

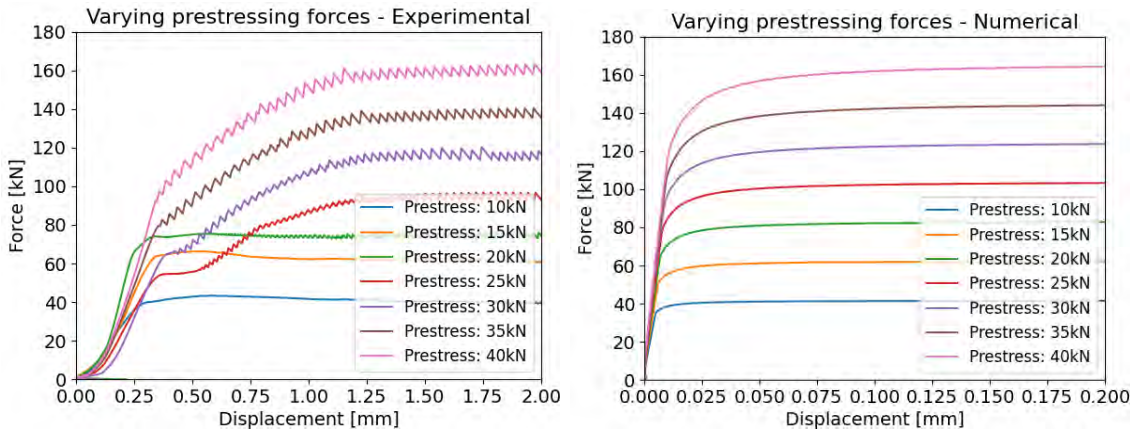

(a) **(b)**

Figure 3.10: Force-displacement responses for different magnitudes of the applied prestressing force on sine variant 3 resulting from the experimental (a) and numerical (b) analysis. Note that the scale of the x-axis differs for the experimental and numerical results.

3.4 Conclusions

All geometries showed promising results during this first experimental phase. The ultimate shear force for the different geometries was similar. However, for the failure mechanism, some differences were visible. As explained above, when a sinusoid connection fails due to sliding, the shear force rises slightly after the linear part is finished if the prestressing force is high enough. These higher deformations can be an indication that the connection is failing and could therefore serve as a warning mechanism. Furthermore, as mentioned in section 3.2.2, the round shapes of the sinusoid connection lead to a better stress distribution and a reduction of high stress concentrations. As stress concentrations are one of the challenges of mechanical joining, reducing that can be highly beneficial.

Regarding robotic manufacturability, the Lego geometry is the hardest to manufacture. The sharp edges and multiple corners make it difficult to manufacture the geometry with the 3D concrete printer, meaning the whole shape must be created by milling. The sinusoid and the dapped-end geometries both can be made with the 3D concrete printer only, as can be seen by the work of Ferguson [12] and Yu [33] for the sinusoid connection and the work of Moretti [24] for a dapped-end connection. Milling may be required for higher precision, but the base geometry can already be created during printing, saving much effort and material.

As already explained, a sinusoid connection can either fracture or slide. These are significantly different failure mechanisms. This makes it possible to adapt the connection completely based on the requirements. All geometries are adaptable to different kinds of elements. However, it is expected that the direction of the layers has a more significant influence on the shear resistance of the Lego shape and the dapped-end shape because the cracks run in a vertical direction and can therefore run through the interface of two layers. As this interface is known to be the weakest link, this is unfavourable. For the sinusoid connection, depending on how the elements are constructed, the layers can be shaped in a sine wave as well, reducing the shear stress on the interface between two layers.

Combining the structural behaviour, the manufacturability, and the adaptability of a connection, it can be concluded that the sinusoid connections seem most promising at this point. Therefore, for the rest of this research, the focus is on this type of geometry. Further research was done on the influence of the wavelength, amplitude, and prestressing force for the two types of failure mechanisms.

Chapter 4

Experimental study on a sinusoid connection

4.1 Introduction

To be able to establish design recommendations for a demountable connection a more detailed analysis of the influence of certain design choices was performed. As explained in paragraph 3.4, the rest of this research focuses on a sine-shaped connection due to its promising results. This chapter presents the experimental analysis of a sinusoid connection. The experimental research was used to analyse the influence of the amplitude, wavelength and prestressing force. Furthermore, the possibilities within digital manufacturing and the possible effect of the interlayer bond strength in printed concrete were analysed. Lastly, the results were used to verify the numerical analysis presented in chapter 5.

4.2 Methodology

To minimize manufacturing deficiencies and to investigate geometries with a more extreme sinusoid shape, a large part of the specimens was cast into formwork. Besides that, two different geometries were manufactured with the 3D concrete printer to see the effect of the interlayer bond strength. For the cast specimens, four different sinusoid geometries were chosen for the experimental analysis, of which two geometries were tested for two different prestressing forces. Furthermore, the specimens that did not show signs of fracture were tested at an increased prestressing force as well. The geometrical properties of both the cast (C) and the printed (P) specimens are given in table 4.1, where each geometry is tested three times.

Table 4.1: Geometrical properties of the specimens and the applied prestress. The definitions of the properties are indicated in figure 4.3.

Specimen	**Amplitude (A) [mm]**	**Wavelength (λ) [mm]**	**Max. angle (α) [deg]**	**Prestress (P/h) [MPa]**
C1	10	200	17.44	0.5
C2	10	100	32.14	0.5
C3	10	66.67	43.30	0.5
C4	20	66.67	62.05	0.5
C5	10	66.67	43.30	2.0
C6	20	66.67	62.05	2.0
P1	10	200	17.44	0.5
P2	2	100	7.162	0.5

Preparation cast specimens

For the cast specimens, the sinusoid shapes were sawn out of styrofoam by hand. The styrofoam parts were covered with a layer of plastic and placed in plywood boxes to create the formwork, similar to the formwork created for the preliminary study. To have an equal water-to-cement ratio for all specimens, the concrete is mixed in a Carat mixer as visible in figure 4.1a contrary to using the pump of the concrete printer as was done in the preliminary study. The specimens were cast on two separate days in three batches per day. For each batch, three mortar beams were cast as well to verify possible differences in concrete strength. A batch was mixed by first adding half of the cement and half of the water, this was mixed for 20 seconds. All dry material left was scraped loose. After that, the rest of the material was added and mixed for 2 minutes. Again, all dry material was scraped loose, after which the concrete was mixed for another 2 minutes. This concrete is poured into the formwork as visible in figure 4.1b.

After pouring, all specimens were covered with plastic. After 24 hours, the formwork of the first half of the specimens was removed to be able to create the second half of the specimens. The specimens from the first day were covered with plastic, and a bucket of water was placed underneath the plastic to increase the humidity, as can be seen in figure 4.1c. The formwork of the specimens cast on the second day was only removed after five days due to closure of the laboratory. By covering both batches with plastic and by adding the bucket of water, an attempt was made to keep the circumstances as equal as possible. Furthermore, differences in strength can be established with the 3-point bending tests and the uni-axial compression tests on the mortar beams.

(a) Concrete mixed in Carat mixer

(b) Concrete poured into form work

(c) Specimens hardening while covered

Figure 4.1: Photos of the preparation of the cast specimens

Preparation printed specimens

The printed specimens were printed with an ABB IRB 1200-5kg-900mm 6-axis robot arm. Concrete is mixed in the Carat mixer, similar to the cast specimens, and poured into a pump located at the back of the set-up, see figure 4.2a. The material used for the printed specimens was two years old, but it was packed in a good way. To be certain about possible material deficiencies, three mortar beams were created and tested for this material as well. The pump was a MAI 2Pump-Pictor with a 10L worm pump. Under the pressure of the pump, the concrete is forced through the hose towards the nozzle. The nozzle, being a round nozzle with a diameter of 15.5mm, is connected to the robot arm. To produce a layer width of 20mm and an average layer height of 6 mm, an average print speed of 70 mm/s and a constant pump pressure resulting in a flow rate of 0.8 l/min were maintained.

A print path of six specimens in a row was programmed. For this print path, it took around 2.5 minutes to complete one layer. The print path was created in a zigzag pattern resulting in solid specimens. The nozzle height and orientation were determined based on the desired sine wave to create a sinusoid shape. The curves between the first and the last layer are interpolated to achieve a smooth transition from a flat layer to a sine-shaped layer. Lastly, to achieve a constant layer width, the print speed depended on the distance of each plane on the print path towards the curve of the previous layer. This print speed varied between 58 mm/s and 88 mm/s.

The upper five millimetres of concrete were milled away to achieve a smoother and more precise interface surface. The milling was done by connecting an AMB 1050 FNE-P milling motor with an 8mm end mill to the robot arm. As mentioned in paragraph 2.3.2, to be able to mill with a lightweight robot arm, the milling should be done in the green-state of concrete. Therefore, the milling was done two hours after printing. According to Ferguson [12], the smoothest surface was achieved when rotating the milling tool at a high RPM an moving the tool over the material slowly. However, due to safety restrictions in the laboratory, the milling tool could rotate with a maximum speed of 3500 RPM. The tool moved over the material at a speed of 25 mm/s. The milling tool moved over all material twice, where the moving direction changed. In the first run, visible in figure 4.2d, a lot of material was milled away, but the material stayed on the specimen. With a soft brush, the excess material was brushed away. A second run was done to ensure the interface is as smooth as possible. After the milling was completed, the specimens were covered with plastic, as can be seen in figure 4.2f.

The first six specimens were printed on Friday. On Monday, a small piece of plastic was placed on all six specimens, and six new specimens were printed on top of the first six, as can be seen in figure 4.2c, to be able to create a specimen with a sinusoid interface on two sides. On Tuesday, the last six specimens were printed, again on top of the previously printed specimens, to keep the interfaces of the specimens as equal as possible. On Wednesday, all specimens were stored together with the cast specimens.

(a) MAI 2 Pump-Pictor

(b) 3DCP Set-up

(c) Printing sine-shaped objects

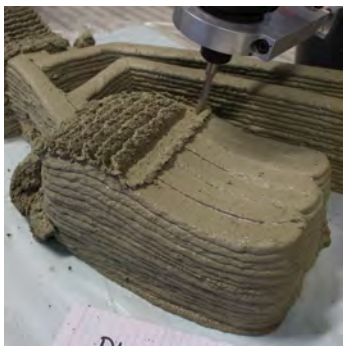

(d) First round of milling

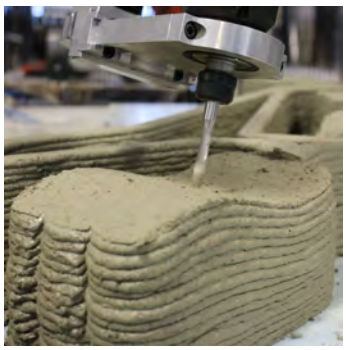

(e) second round of milling

(f) Printed specimens hardening while covered

Figure 4.2: Photos of the preparation of the printed specimens

Direct shear test

The direct shear tests were performed in the same set-up as explained in section 3.3.1. However, for this analysis, the LVDTs were positioned such that the vertical displacement of the steel plate on top of the middle specimen was measured. This displacement is equal to the vertical displacement of the top of the middle specimen itself. The steel plate had a width of 100mm and a thickness of 20mm.

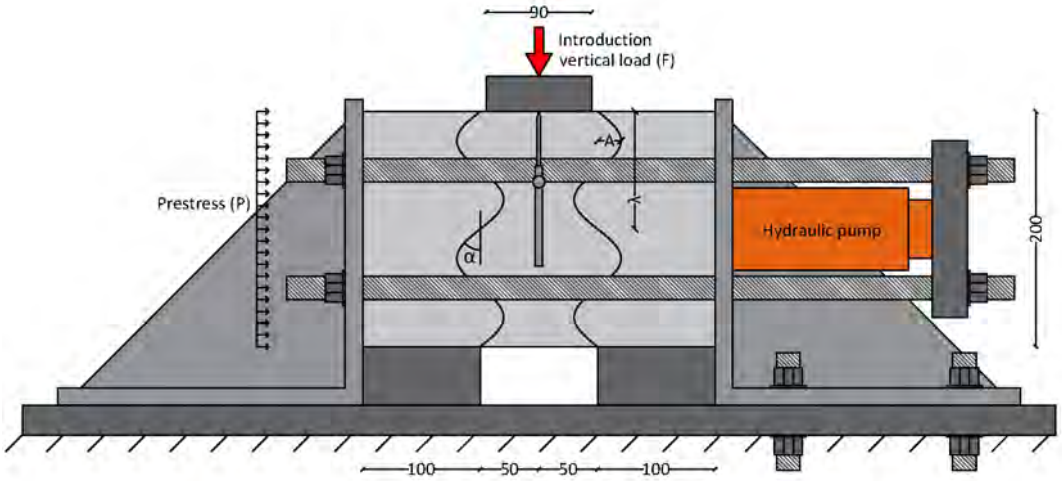

Figure 4.3: Test set-up double shear push-out test with the displacement measured at the top. The dimensions are in millimetres, and the maximum angle, the amplitude, and the wavelength of a sinusoid geometry are indicated with the symbols α, A, and λ respectively.

Surface analysis

The surface of three cast and four printed specimens was measured using a scanCONTROL 2900-100 from Micro-Epsilon to measure the surface roughness and the deviations within the surface. The distance from the scanner to the specimens was between 200 and 250 mm, which is within the optimal range of the scanner. The profile extracted from each measurement can be separated into higher and lower frequencies, where the high frequencies indicate the roughness and the lower frequencies the waviness of the profile. This results in the three profiles illustrated in figure 4.4 defined by Leach [17].

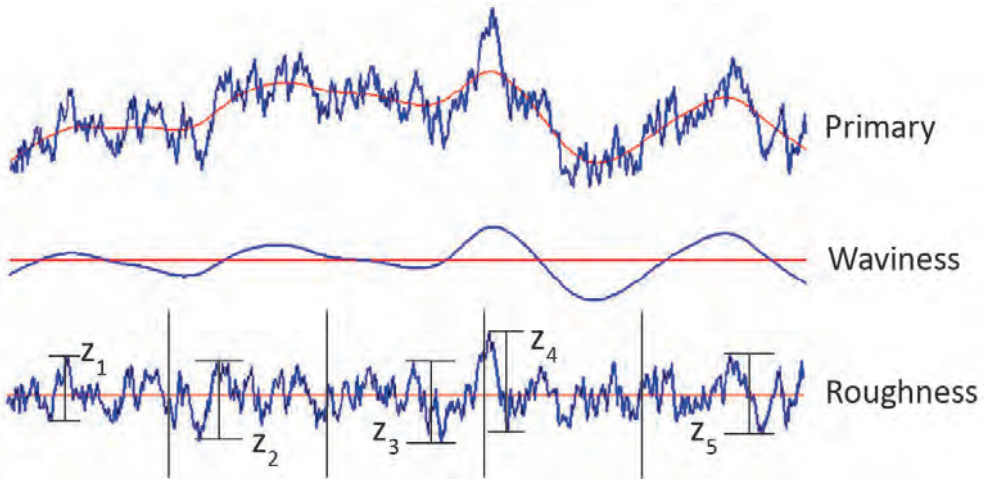

Figure 4.4: Primary, waviness, and roughness profiles adapted from the work of Leach [17].

The roughness profile can be used to determine various roughness parameters. within this research, the mean peak-to-valley height was used, as recommended by Mohamad et al. [22]. The mean peak-to-valley height R_z as described by Santos et al. [28] can be determined with equation 4.1, where the evolution length is divided into five parts and z_i equals the peak-to-valley height of each part as indicated in figure 4.4.

$$R_z = \frac{1}{5}\sum_{i=1}^{5} z_i \tag{4.1}$$

4.3 Results

The material properties of all six batches used for the cast specimens and older material used for the printed specimens were determined with a 3-point bending test and a uni-axial compression test. The results of these tests are given in table 4.2. Within the cast specimens, the maximum deviation is about 6.5% and 5% for the flexural strength and compressive strength, respectively. No significant differences in the shear test are expected due to differences in material properties as these deviations are similar to the deviations within a single batch, as presented in table 4.2. The older material used for the printed specimens has a slightly lower flexural and compressive strength with a deviation of about 10 % for both properties. This is also not a significant deviation, especially because the printed specimens failed due to sliding, meaning that the fracture properties did not influence the maximum shear force.

Table 4.2: Flexural strength and compressive strength of the six different batches of concrete used for the cast specimens (1-6) and the material used for the printed specimens (A)

Concrete batch	Flexural strength [MPa]	Relative stdv. [%]	Compressive strength [MPa]	Relative stdv. [%]
1	4.99	5.86	38.06	3.43
2	5.15	11.66	38.58	5.53
3	5.40	3.79	37.55	4.29
4	5.07	6.01	40.59	3.27
5	4.99	6.02	40.01	2.33
6	4.82	2.12	37.19	6.42
A	4.51	6.40	35.34	7.24

During the direct shear test, two failure responses were observed. C1, C2, P1 and P2 failed due to sliding along the interface, as visible in figure 4.5a and C3 until C6 failed due to fracture, shown in figure 4.5b. First, the results of the geometries that failed due to sliding are presented, after which the results of the other geometries are discussed.

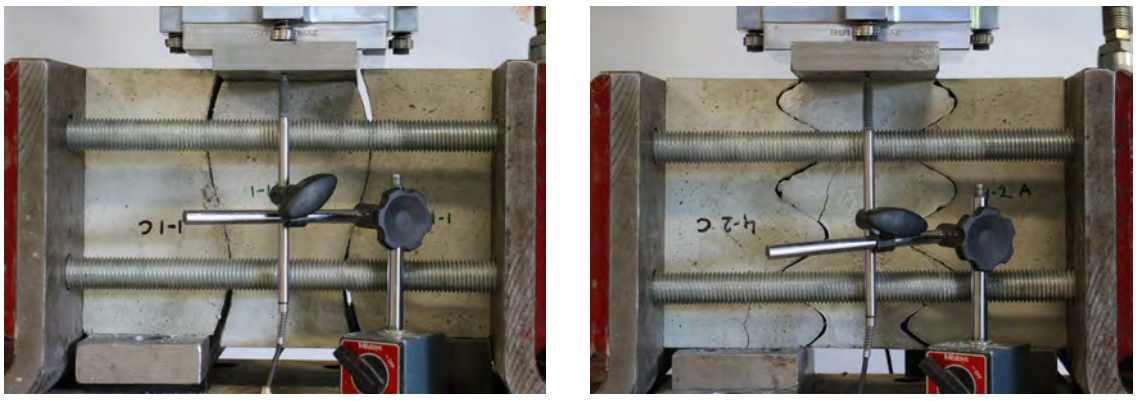

(a) Sliding along the interface **(b)** Fracture

Figure 4.5: Failure mechanisms observed in the experimental analysis

Sliding along the interface

The mechanical responses of the geometries that failed due to sliding are illustrated in figure 4.6 by plotting the applied vertical force versus the vertical displacement of the middle specimen. The vertical displacement is determined by averaging the vertical displacement measured at the front and the back of the specimen. The upward displacement up to 0.5mm due to the application of the prestressing force is not included within the force-displacement responses. Figure 4.6a illustrates the load-displacement responses of specimens C1 and P1. It can be observed that there are no significant differences between the printed and the cast specimens. The ultimate shear force measured for the cast specimens is slightly higher than for the printed specimens, which can be explained by the fact that the surface roughness of the interfaces of the cast specimens was higher than for the printed specimens, as is presented in section 4.3.1. Therefore, the results show that printing specimens compared to casting did not influence the mechanical response, but the surface roughness did.

Figure 4.6b shows the load-displacement response of the same geometry as figure 4.6a, but a higher prestress is applied. The tests showed that if the prestress is increased by a factor of two, the ultimate shear forces increase by around seventy percent. This increase is similar to the results measured in the preliminary analysis, visualised in figure 3.9, which showed a linear relationship between the ultimate shear force and the applied prestress.

The load-displacement responses of specimens C2 and P2 are illustrated in figures 4.6c and 4.6d, respectively. When looking at all load-displacement responses, it can be seen that if either the amplitude increases or the wavelength decreases, the ultimate shear force increases. If these ultimate forces are compared to the maximum angle, the sinusoid wave makes with the vertical axis, as listed in table 4.1, it can be concluded that the ultimate shear force increases with an increasing maximum angle. The nature of this relationship will be further analysed in the numerical analysis, described in section 5.3.

The response of specimen C2_2 differs from the other load-displacement responses as it first reaches a relatively high peak before reaching a plateau similar to the other specimens. This peak can be explained by the irregularities within the interface. A small bump in the interface prevented the interfaces from sliding along each other. At a force of 105kN, the irregularity broke off, after which sliding was not prevented anymore, and the force dropped to stabilise at a plateau of around 55kN.

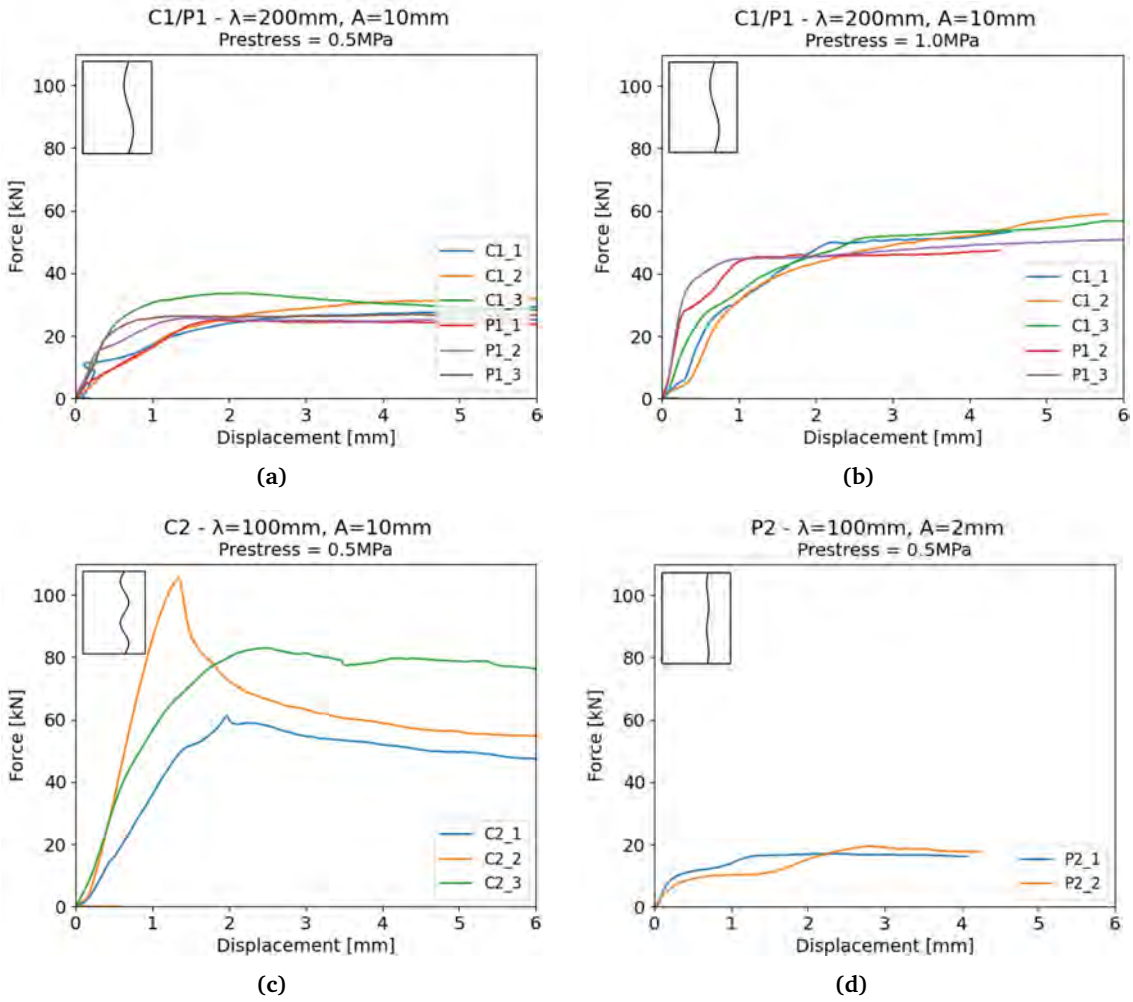

Figure 4.6: Experimental load-displacement response of the three geometries that failed due to sliding along the sinusoid interface

Fracture

Figure 4.7 illustrates the mechanical response of the geometries that failed due to fracture by plotting the applied vertical force versus the vertical displacement of the middle specimen. Figures 4.7a and 4.7b present the load-displacement responses of specimens C3 and C4, respectively. Figures 4.7c and 4.7d show the load-displacement responses of the same geometries but with a higher applied prestress. The different specimens with equal properties present similar results. When comparing C3 and C4, it can be seen that a higher amplitude results in a lower ultimate shear force. Furthermore, for a lower amplitude, the shear resistance makes a sudden drop as soon as the peak force is reached, while the resistance of a geometry with a higher amplitude (C4) makes a significantly smaller drop.

When looking into the effect of prestress, thus comparing C3 with C5 and C4 with C6, it can be seen that a higher prestress increases the ultimate shear force. However, this effect is more significant for the geometry with a higher amplitude. The ultimate shear force of a geometry with an amplitude of 10mm (C3 and C5) increases only about 15%. For the geometry with an amplitude of 20mm (C4 and C6), this was about 85%. This could indicate that the cracks that developed in the specimens with a higher amplitude were mainly caused by horizontal stresses. These stresses are then counteracted by the higher prestress in C6. The cracks developed in the specimens with a smaller amplitude may have been caused mostly by vertical stresses, being shear stresses, as these stresses are not counteracted by the prestress. However, the cracks visible during the experiments did not differ significantly between

the different geometries. A more detailed analysis of this phenomenon is done in chapter 6, where the experimental results are compared to the numerical results.

The lower stiffness of C3_2 in figure 4.7a could be caused by an extra crack occurring at the bottom of the most left specimen, giving more room to rotate.

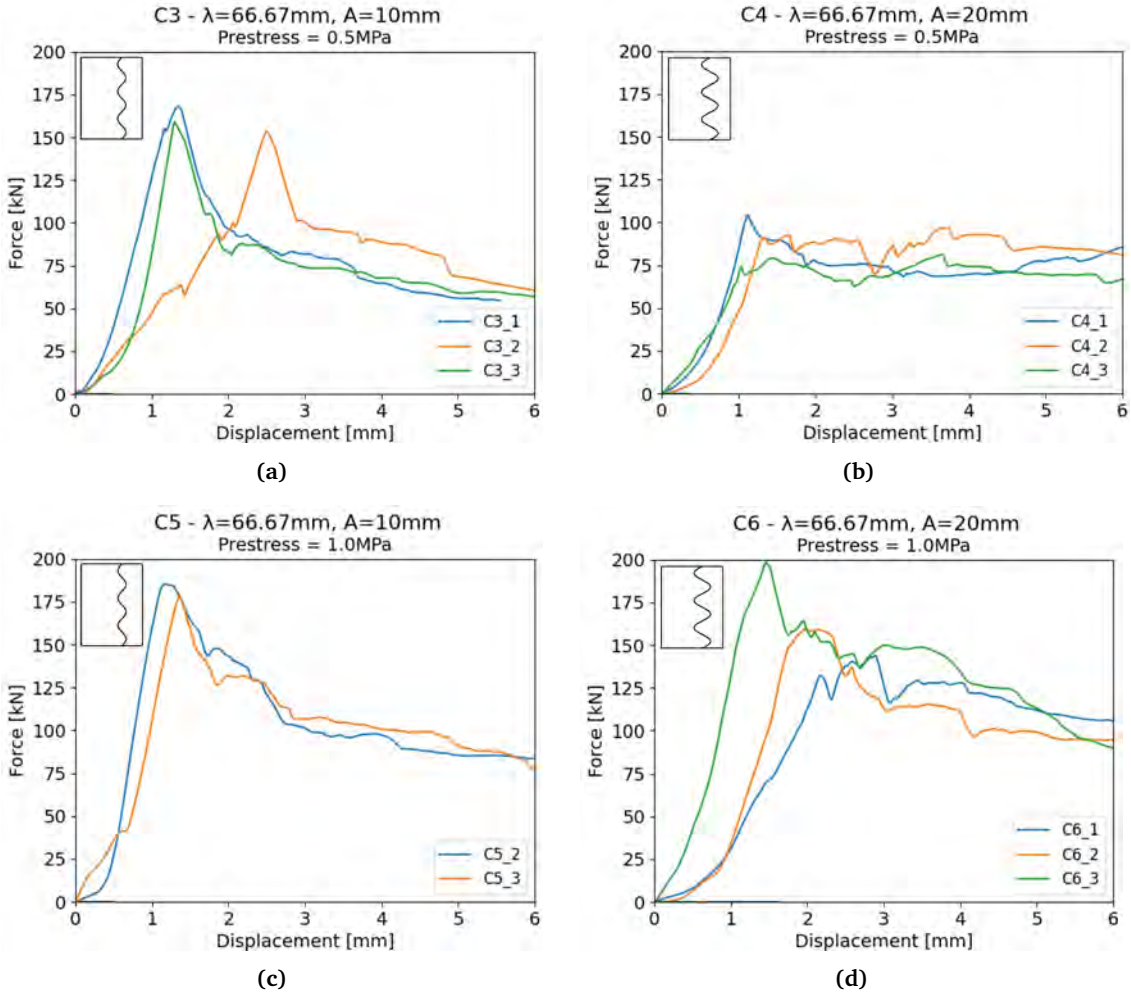

Figure 4.7: Experimental load-displacement response of the two geometries prestressed with two different forces that failed due to fracture

4.3.1 Surface roughness

Figure 4.8 shows the primary profile and the waviness in the top figure and the roughness profile in the bottom figure of a section of one of the cast specimens (C1_1). The three profiles are determined as explained in section 4.2. Note that the z-coordinate represents the distance from the laser to the specimen. From the waviness profile, it can be observed that the deviations within the surface are around 2 millimetres. The deviations of the other measured specimens were of the same order. With the roughness profile, the mean peak-to-valley height (R_z) was determined according to equation 4.1. R_z was equal to 0.57mm and 0.48mm for the cast and printed specimens, respectively.

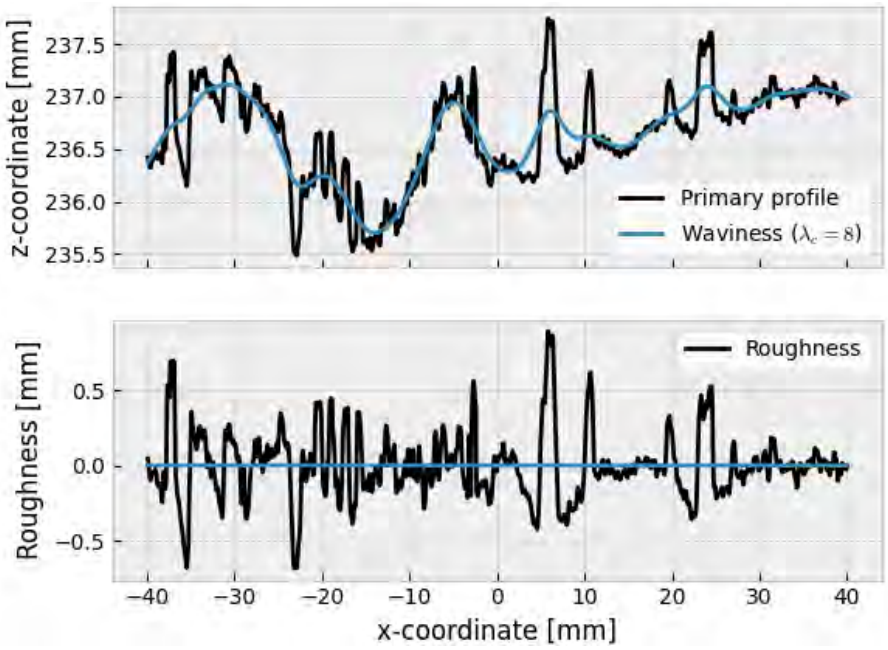

Figure 4.8: Results of the surface analysis of one of the cast specimens. The top graph illustrates the primary profile and the waviness. The bottom image shows the roughness profile derived by suppressing the long-wave component using a high-pass filter.

Chapter 5

Numerical analyses on a sinusoid connection

5.1 Introduction

Additional to the experimental analysis, multiple numerical analyses were performed. The goal of the numerical analyses was to get a better understanding of the behaviour of the connection. Furthermore, the influence of varying the wavelength, amplitude and prestress on the mechanical behaviour was further analysed. First, a finite element analysis, including cohesive zone modelling, is presented. After that, a simpler finite element analysis for cases that fail due to sliding is presented. Lastly, the connection is evaluated using a strut-and-tie analysis.

5.2 Finite element analysis including cohesive zone modelling

5.2.1 Methodology

The numerical analysis is performed as a 2 dimensional linear elastic finite element analysis (FEA) with the commercial software package ABAQUS standard. Similar to the method used for the preliminary study presented in paragraph 3.2.1, the friction between the elements was defined as surface-to-surface contact using hard contact as normal behaviour and the penalty method as tangential behaviour. Based on the results of the preliminary study, the friction coefficient was defined as 0.63, as explained in paragraph 3.3.2.

In addition to the Morh-Coulomb model, discrete cracking was simulated. This was done using cohesive zone modelling. Cohesive zone modelling is based on a combination of 3-node linear plane-stress continuum elements describing the elastic bulk material surrounded by 4-node cohesive interface elements describing the fracture behaviour. This is modelled by constructing a mesh of continuum elements within Gmsh, reducing all these 3-node elements by one percent and using the space in between for the interface elements. The behaviour of the interface elements is described by a mixed-mode damage model as presented by Cid Alfaro et al. [7]. This damage model is implemented in ABAQUS by means of a user-subroutine.

In the interface damage model, the traction (t_i) is related to the relative displacement across the interface (v_i) with the constitutive relation given in equation 5.1.

$$t_i = (1-d)K\delta_{ij}v_i - dK\delta_{ij}\delta_{1j}\langle -v_1\rangle \tag{5.1}$$

This equation shows that the stiffness reduces when damage increases. The second term of the equation prevents crack penetration of two opposite crack faces, where the Macauley brackets are defined as $\langle x\rangle = \frac{1}{2}(x+ \mid x \mid)$.

Within equation 5.1, the damage d evolves with deformation and is therefore dependent on a deformation history parameter κ. The shape of $d(\kappa)$ corresponds to the traction-separation law, which is described with a linear softening branch as visualised in figure 5.1. The traction-separation law describes how the interfacial stiffness K decreases with an increase of damage, where the damage varies from d=0 (where damage is initiated, corresponding to $\kappa = v^0$ in figure 5.1) to d=1 (where damage is completed, corresponding to $\kappa = v^u$ in figure 5.1). The damage process can be described with the ultimate traction or interfacial strength (t^u) and the fracture toughness (G_c), where the fracture toughness equals the area under the traction-separation curve. A backward Euler approach is used for the incremental update procedure, where time t_{n+1} is used to evaluate the model variables in the interfacial integration points. The time t_{n+1} is determined by $t_{n+1} = t_n + \Delta t_{n+1}$, and it is assumed that the corresponding model variables at the time step t_n are known. In a displacement-based analysis, this leads to the relative displacements across the interface ($\boldsymbol{v}_{n+1}$), which are used as input for the global analysis on the system level.

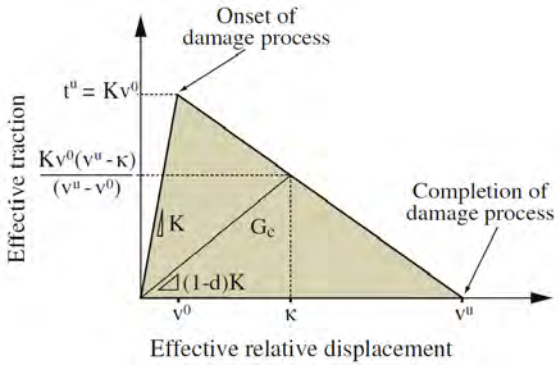

Figure 5.1: Traction-separation law as described by Cid Alfaro et al. [7].

Material properties

As the damage model distinguishes between mode I and mode II contributions, to be able to describe the full damage model, the interfacial strength in mode I and mode II and the fracture toughness in both modes should be determined. The mode I properties were defined by calibrating a numerical model of a four-point bending test on the experimental results of the same test performed by Versteege in 2023. For these tests, 55 specimens with a cross-section of 40x40mm were subjected to a four-point bending test with a span of 210mm. The distance between the two loading points was 70mm. The specimens were printed with the material Weber 145-2. A numerical model was created for this set-up, and the mode I parameters were adjusted until the load-displacement responses matched the experimental results. The Young's modulus of the continuum elements is determined in the same way and validated with literature. The results of this analysis are presented in appendix A.

For simplicity, the critical energy release rate in mode II ($G_{II,c}$) was based on the results of Reinhardt and Xu [27], where $G_{II,c}$ for concrete with a similar compressive strength was measured to be equal to 0.24 N/mm. The interfacial strength in mode II was determined based on research performed by Turon et al. [32]. It was stated that if linear elastic fracture mechanics applies, the ratio between mode I and mode II interfacial strength could be determined by equation 5.2. This relation was derived from the concept that the time derivative of the damaged area always has to be non-negative as no healing is predicted. For the exact derivation, the reader is referred to [32].

$$t_2^u = t_1^u \sqrt{\frac{G_{II,c}}{G_{I,c}}} \tag{5.2}$$

Linear elastic fracture mechanics is applicable if the material behaves purely brittle. Concrete is not a pure brittle material, but for simplicity, the value obtained from equation 5.2 is used, and both mode II properties were validated with the results of the preliminary study shown in paragraph 3.3.2 to validate

whether the assumptions made were reasonable. For this validation, the crack pattern and the type of failure (fracture or sliding along the sinusoid interface) were observed.

Furthermore, the elastic stiffness K of the interface elements is chosen to be relatively high. This is to ensure the interface elements do not influence the elastic behaviour of the material and only start deforming when the plastic regime is reached. However, when the elastic stiffness is too high, numerical problems arise. Therefore, a value of $1e^5$ was chosen. A small variational study was performed to determine the viscosity (η). For the definition of η, the reader is referred to [7]. A small value of η gives the most precise results but increases the computational time and can give convergence problems. Therefore, the largest value for η that does not influence the results significantly is searched for. Lastly, the Poisson's ratio was taken from the Eurocode EN 1992-1-1 [26]. All properties are listed in table 5.1.

Table 5.1: Material properties used in the numerical analysis

Parameter	Symbol	Value	Unit
Properties continuum elements			
Young's modulus	E_c	32.000	[N/mm^2]
Poisson's ratio	υ_c	0.2	[-]
Properties interface elements			
Elastic stiffness	K	10^5	[N/mm^3]
Ultimate traction mode I	t_1^u	2.5	[N/mm^2]
Ultimate traction mode II	t_2^u	5.0	[N/mm^2]
Fracture toughness mode I	$G_{I,c}$	0.06	[N/mm]
Fracture toughness mode II	$G_{II,c}$	0.24	[N/mm]
Relaxation parameter	η	10^{-4}	[s]
Factor to prevent damage to be completed	ϵ	10^{-12}	[-]

Geometry and boundary conditions

The geometry and boundary conditions of the numerical analysis are visible in figure 5.2. The dimensions (given in millimetres) equal the dimensions used in the experimental analysis. As the experimental test set-up is symmetrical, in the numerical analysis, only half of the set-up is modelled. As shown in figure 5.2, a symmetry axis is modelled on the right side of the model. The prestressing force P is applied as a surface pressure load, and the analysis is performed deformation controlled, so the vertical force F is modelled as a deformation downwards. The magnitude of the prestressing force P, the amplitude A and wavelength λ, as indicated in figure 5.2, were varied to find the influence of different parameters.

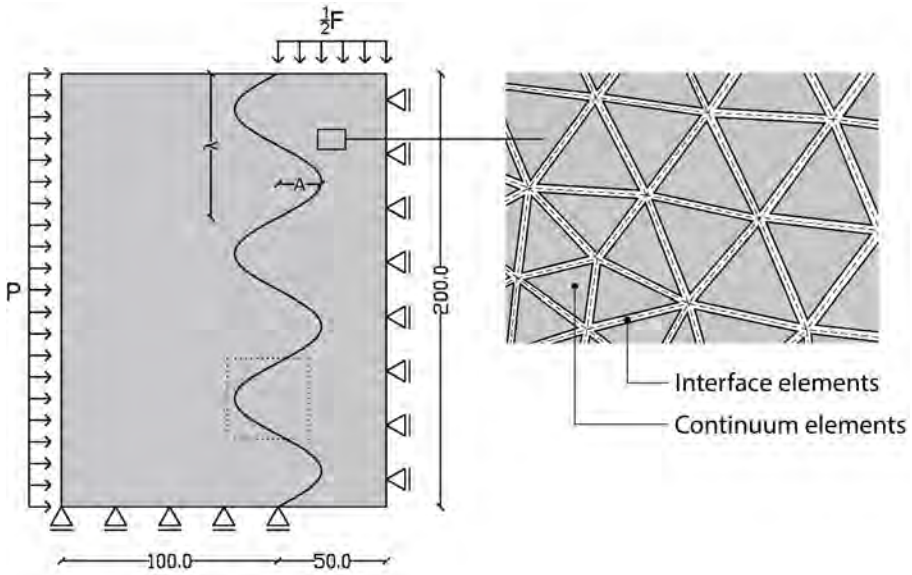

Figure 5.2: Dimensions (in millimetres), applied loading and boundary conditions on a sinusoid connection used for the numerical analysis. The square box indicates the area for which the mesh is visible in figure 5.3.

Mesh refinement study

The finite element discretization can influence the fracture response, as cracks can only run through the interface elements. This influence can be minimized by choosing a sufficiently fine mesh. However, if the mesh is too fine, the stiffness of the interface elements will influence the elastic response of the finite element model [6]. Therefore, three different meshes are considered, partly illustrated in figure 5.3. The area visible is indicated in figure 5.2. In table 5.2, the number of continuum and interface elements for all three meshes are listed.

(a) Coarse mesh **(b)** Intermediate mesh **(c)** Fine mesh

Figure 5.3: Part of the three different meshes used to determine the influence of the numerical discretization. Figure 5.2 indicates which part is visualized.

Table 5.2: Number of elements for the three different meshes

Mesh	**Part 1**		**Part 2**		**Total**
	Continuum	Interface	Continuum	Interface	
Coarse	12683	18824	7957	11749	51213
Intermediate	19647	29220	14272	21161	84300
Fine	28463	42383	25450	37845	134141

The results of the mesh refinement study are visualised in figure 5.4 showing the deformed shape and figure 5.5 showing the force-displacement responses. The force-displacement response presents the vertical force on the right part against the vertical displacement at the top of this part. The crack patterns in the meshes are slightly different, resulting in small deviations in the force-displacement responses. This is expected, as the cohesive elements are not in the exact same places. However, the global behaviour for all three meshes is similar, with cracks in similar places and force-displacement responses with only small deviations. Therefore, the coarse mesh will be used for the forthcoming simulations to reduce the computational time.

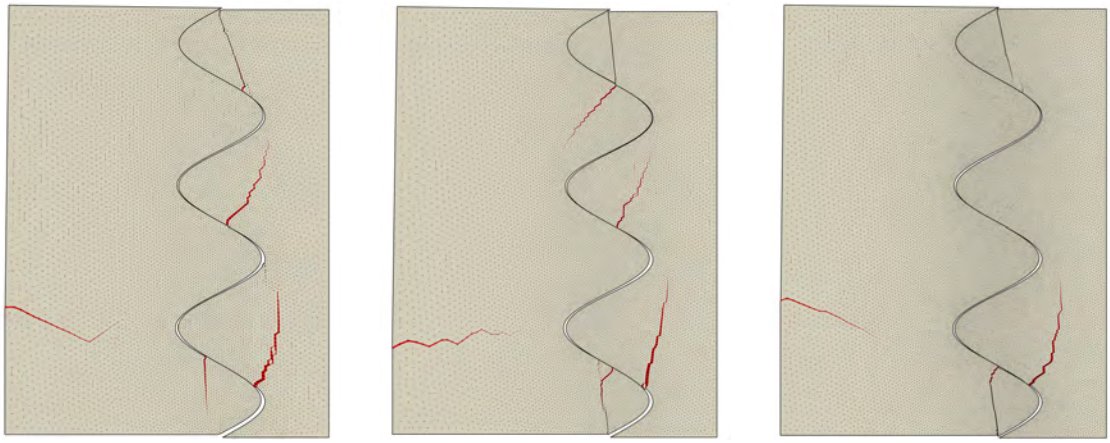

(a) Coarse mesh **(b)** Intermediate mesh **(c)** Fine mesh

Figure 5.4: Deformed shapes of three different meshes, for which the deformation is scaled with a factor 5.

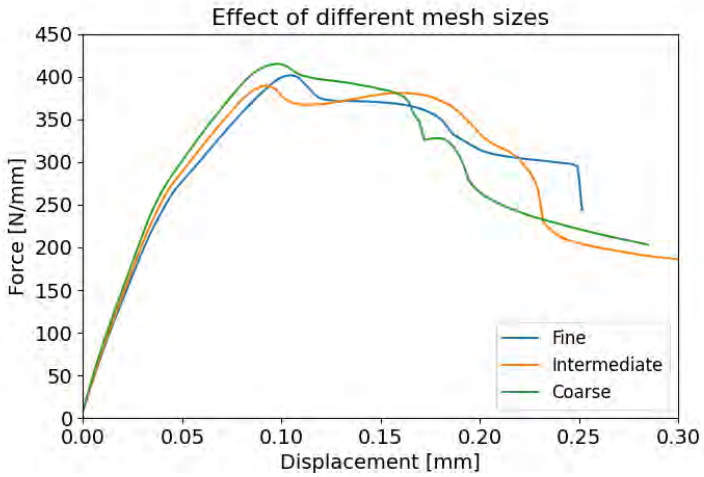

Figure 5.5: Force-displacement responses of three different meshes for a geometry with a wavelength of 66,67mm and an amplitude of 20mm

5.2.2 Results

Three different failure mechanisms were observed within the various numerical simulations performed, visualised in figure 5.6. This figure presents the maximum principle stresses plotted on the deformed shape. The deformations are scaled with a factor of ten. Overall, the force applied on the top right is transferred through the most horizontal parts of the sinusoid geometry towards the support on the lower left. When the maximum angle of the sinusoid geometry is relatively small, as visible in figure 5.6a, the connection fails due to sliding, similar to the experimental results. The curvature in the flow of forces leads to some small splitting tensile stresses. When the angle of the sinusoid geometry becomes larger, these splitting tensile stresses increase and can lead to fracture, as visible in figure 5.6b.

Figure 5.6c visualises a third failure mechanism. Instead of cracks due to splitting tensile stresses, multiple cracks developed from the top to the bottom of the notches. The two opposite crack faces are still touching but have slid relative to each other, indicating a mode II crack. For both cases, the mode mixity parameter β can be determined by equation 5.3 as defined by Turon et al. [31], where β=0 reflects pure mode I loading and β=0 relates to pure mode II loading.

$$\beta = \frac{v_{sh}}{v_{sh} + \langle v_1 \rangle} \tag{5.3}$$

For the second failure mechanism (b), β was determined for crack initiation and crack propagation. For crack initiation, β was equal to 0.33 measured within the interface element where the crack was imitated. For crack propagation, β varied between 0.11 and 0.44, measured in various interface elements surrounding the crack tip. Both crack initiation and crack propagation indicate a mode I dominated crack. For the last failure mechanism (c), the mode mixity parameter β within the interface elements of the cracks varied between 0.83 and 0.98, corresponding to mode II loading.

The force-displacement responses of the three failure mechanisms are given in figure 5.7 by plotting the vertical shear force against the vertical displacement at the top of the right part. The three different cases have significantly different responses. If sliding occurs, the force increases until a constant plateau is reached. If the connection fails due to splitting tensile forces, the cracks develop one by one, and the shear force decreases gradually. In the last case, the three cracks develop simultaneously, and the shear resistance suddenly drops. Section 6.2 presents the occurring cracks in relation to the force-displacement responses in more detail.

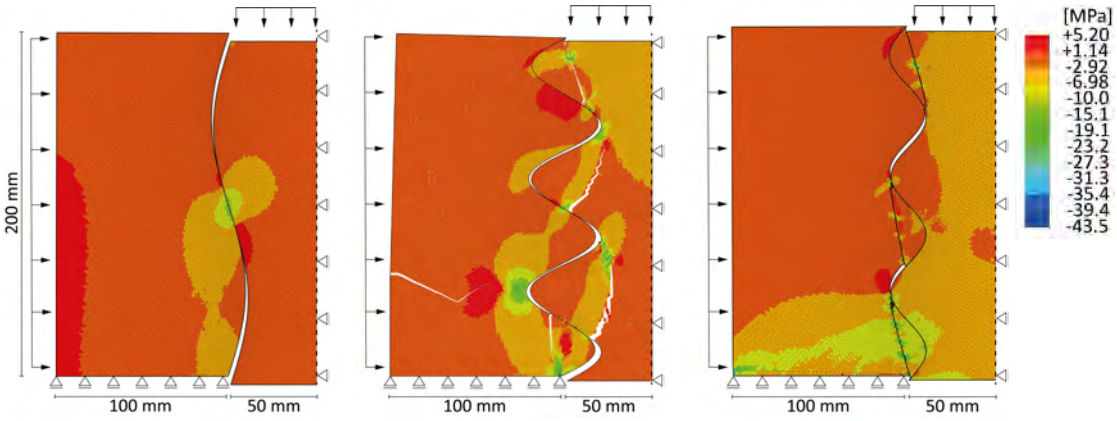

(a) **(b)** **(c)**

Figure 5.6: Maximum principle stresses plotted on the deformed shape. Note that the deformations are scaled with a factor of 10

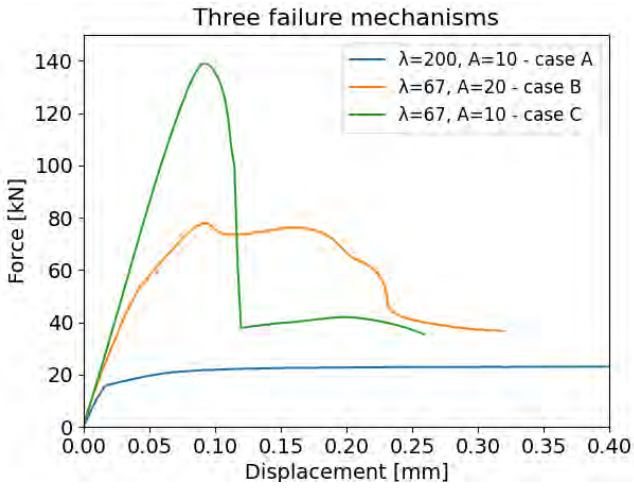

Figure 5.7: Force-displacement response of the three different failure mechanisms in which the vertical shear forces are plotted against the vertical displacement

5.3 Linear-elastic finite element analysis

In the previous section, it was explained that not all geometries fail due to fracture. If no cracks occur, the cohesive elements used to model discrete cracks can be excluded from the model. Excluding these elements significantly reduces the computational time, making it easier to perform more analyses. In both the experimental analysis and the numerical analysis including cohesive elements, it was confirmed that the connection failed due to sliding if the maximum angle does not exceed 32 degrees. This value is with the assumption that the prestress has a maximum value of 2.0 MPa. Therefore, the geometries that fulfil these characteristics are further analysed using a linear-elastic finite element model without cohesive elements. The analysis is similar to that performed during the preliminary study as explained in section 3.2.1.

5.3.1 Results

The results are plotted as data points in figure 5.8 by plotting the vertical slip-out force versus the maximum angle of the sinusoid geometry, indicated with α in figure 5.9. As mentioned in section 4.3, the experimental results already indicated that a higher maximum angle results in a higher slip-out force, which is visible in figure 5.8 as well. In figure 5.9, the two forces applied on the geometry, the shear force (F) and the prestressing force (P), are decomposed into a component normal to the surface and a component parallel to the surface. According to the Coulomb friction theory, the shear stress can be determined with equation 5.4. The stresses in this equation can be replaced by the applied forces.

$$\tau = \sigma tan(\phi) + c \tag{5.4}$$

It is assumed that there is no cohesion within the connection. The shear force could thus be determined by multiplying the normal force with the tangent of the friction angle, being the friction coefficient μ. Therefore, the two normal components in figure 5.9 multiplied by the coefficient of friction should equal the two shear components, as presented in equation 5.5. This equation can be solved for F, resulting in equation 5.6. Note that this equation only holds if $cos(\alpha) - \mu \cdot sin(\alpha) > 0$. If that is not the case, the normal component of the vertical force F_{slip} multiplied with the friction coefficient is always larger than the shear component of this force, independent of the magnitude of the force. Therefore, no slip-out behaviour will occur and the force will increase until the connection fails due to fracture. This does not mean that if equation 5.6 holds, no fracture can occur, as the stresses within the connection can still exceed the maximum stresses of the material used.

The results of this equation are plotted in figure 5.8 by the lines and follow the Abaqus results well. As can be seen in the graph, equation 5.6 overpredicts the slip-out force if this force becomes high. This can be explained by deformations within the concrete due to the higher force. If the Young's modulus in the numerical simulation is infinitely high, the numerical results correspond to the results of equation 5.6.

When taking a closer look at the equation, it can be seen that there is a linear relation between the slip-out force and the prestressing force, keeping the angle and the friction coefficient constant. Furthermore, no shear resistance is present when the prestressing force is zero. This corresponds to the findings from the preliminary analysis shown in figure 3.9 in section 3.3.2.

$$F_{slip} \cdot cos(\alpha) - P \cdot sin(\alpha) = F_{slip} \cdot \mu \cdot sin(\alpha) + P \cdot \mu \cdot cos(\alpha) \tag{5.5}$$

$$F_{slip} = \frac{P \cdot \mu \cdot cos(\alpha) + P \cdot sin(\alpha)}{cos(\alpha) - \mu \cdot sin(\alpha)} \tag{5.6}$$

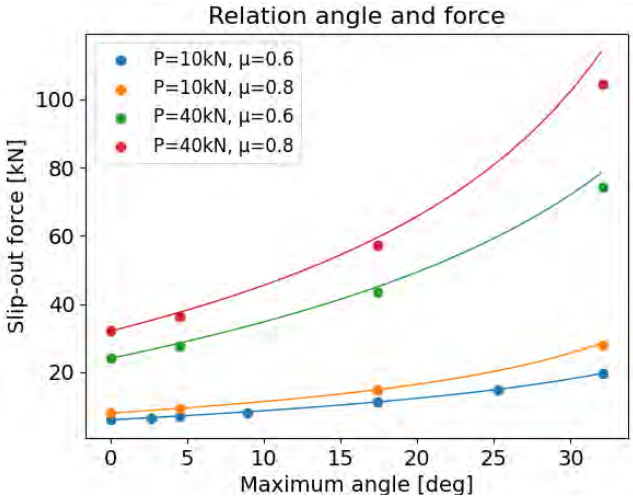

Figure 5.8: The slip-out force for different maximum angles of the sinusoid geometry for two different prestressing forces (P) and two different friction coefficients (μ). The data points are the results extracted from Abaqus, and the lines are created using equation 5.6.

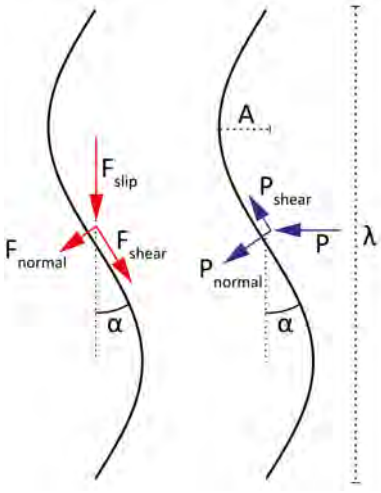

Figure 5.9: decomposition of the shear force (F) and the prestressing force (P) on the sinusoid surface.

5.4 Strut-and-Tie analysis

Strut-and-tie modelling is a method to simplify the flow of forces as triangulated models. The method uses truss analogy and is usually applied to non-standard elements or parts of elements, like corbels. Especially the sinusoid connections that fail due to fracture can be seen as a corbel in some form. Therefore, the connection can be analysed with a strut-and-tie model. This model is visualised in figure 5.10 for two different amplitudes. In this illustration, the red dotted line is the compressive strut, and the blue line is the tension tie.

With this model, the tension force in the tie can be calculated for a particular force F and angle ϕ. This tension force, containing all splitting tension stresses, can result in failure of the connection when it becomes too high. The angle ϕ can be determined with equation 5.7 based on trigonometry, where λ equals the wavelength and A the amplitude.

$$\phi = tan^{-1}(\frac{0.75\lambda}{0.5A}) \tag{5.7}$$

With the angle ϕ, the force F can be decomposed into a compressive force in the strut and a tension force in the tie. This tension force can be calculated with equation 5.8.

$$F_t = \frac{F}{tan(\phi)} = \frac{2A}{3\lambda} \cdot F \tag{5.8}$$

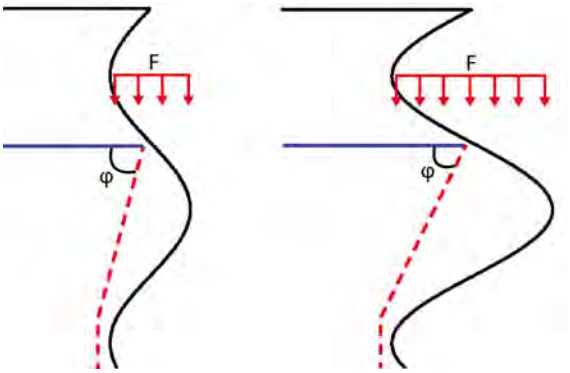

Figure 5.10: Visualisation of a strut-and-tie model of a sinusoid connection. The strut is visualised as a red dotted line, and the tie as a solid blue line.

From equation 5.8, it can be concluded that for a particular applied shear force F, a higher amplitude leads to a higher tension force. Therefore, if this tension force is governing for failure of the connection, a higher amplitude leads to a lower ultimate shear force. The wavelength is also included in equation 5.8 as a smaller wavelength results in a larger tension force. However, the wavelength influences not only the magnitude of the tension force but also the area over which this force is divided and the number of notches in the complete connection (assuming a constant height). A smaller wavelength results in a smaller area over which the tension force can be divided, resulting in higher stresses. But a smaller wavelength also results in more notches within the connection. Therefore, the total applied shear force can be divided over more notches; thus, the tension force at each individual notch becomes smaller. It is, however, unknown how the applied shear force is divided over the different notches. If it is assumed that the shear force is divided equally over all notches, meaning that the tension force F_t can be divided by λ/h, the tension force for each notch can be determined with equation 5.9.

$$F_{t,notch} = \frac{2A}{3\lambda} \cdot F \cdot \frac{\lambda}{h} = \frac{2A}{3h} \cdot F \tag{5.9}$$

This equation suggests that the wavelength does not influence the tension force for the individual notches, although it still influences the area over which the force is divided. However, if all applied forces are assumed to be transferred through one notch only, equation 5.8 still applies for the maximum tension force of one notch. This is a significant difference, and the truth should be somewhere in between, meaning that equation 5.8 gives the upper bound of the tension force and equation 5.9 the lower bound. Both equations imply that a smaller wavelength results in higher tension stresses, as the area over which the tension force can be divided is smaller for a smaller wavelength. But the magnitude of this effect depends on the division of the shear force over the different notches.

looking at figure 5.10 the ultimate force could also be determined by looking at the bending moment caused by the force and the lever arm, instead of determining the magnitude of the tension force via a strut-and-tie model. The bending stress within the connection for a certain force F can be calculated with equation 5.10, where the factor x can be between 1 and λ/h number of notches, depending on how the force is distributed. This equation shows similar effects of the amplitude and wavelength on the ultimate force, but gives a stress instead of a tension force, making it possible to determine the point of failure.

$$\sigma_b = \frac{My}{I} = \frac{F \cdot \frac{1}{2}A \cdot \frac{1}{2}\lambda}{x \cdot \frac{1}{12} \cdot b \cdot \lambda^3} \tag{5.10}$$

Chapter 6

Comparison of experimental and numerical results

This chapter presents a comparison of the experimental and numerical results as presented in the previous chapters. Both the experimental analysis and the numerical analysis including cohesive zone modelling presented similar failure mechanisms, being either sliding or fracture, for the different geometries tested. In this chapter, a distinction has been made between the geometries that failed due to sliding along the sinusoid interface and those that failed due to fracture.

6.1 Sliding along the sinusoid interface

As already explained in section 5.3, no cohesive elements are required for geometries which fail due to sliding. Therefore, the numerical results presented in this section are obtained with a linear elastic FEA excluding cohesive elements. Figure 6.1 presents the deformations of the experimental and numerical analysis, where the numerical results are plotted over the right half of the experimental results. Note that the deformations of the numerical results are scaled with a factor of ten. It can be seen that the type of deformation of both the experimental and numerical results are similar.

Figure 6.2 presents the load-displacement responses of geometry C1. The experimental results are presented in black, and the numerical results are in red. As can be seen, both analyses show a bilinear relationship where the shear force first increases, after which a plateau is reached. The friction coefficient assigned to the surface-to-surface contact within the numerical analysis significantly influences the slip-out force. The red line is the load-displacement response for a friction coefficient of 0.75. To match the slip-out force of the experimental results, the friction coefficient was varied between 0.63 and 0.87 (the red hatched area). The actual friction coefficient is highly dependent on the roughness of the surface. Mohamad et al. [22] analysed the friction coefficient in relation to the surface roughness. For a mean peak-to-valley height (R_z) of 0.62mm a friction coefficient of 0.84 was found. As presented in section 4.3.1, the roughness parameter R_z for the cast and printed specimens was 0.57mm and 0.48mm, respectively. This indicates that a friction coefficient between 0.63 and 0.87 is to be expected.

As shown in figure 6.1, there is a significant difference in stiffness of the linear part between the experimental and numerical results. In the numerical results, the plateau is reached after 0.015mm, while for the experimental results, this is only at around 1.5mm. The deviations within the interface surface of the experimental specimens can explain this difference. As mentioned in section 4.3.1, the waviness profile of the interface surface showed deviations of about 2mm. This is in the same order as the differences in stiffness between the numerical and experimental results. Furthermore, the linear part should be in correspondence with Hooke's law. Therefore, with a Young's modulus of 32.000MPa and a force of 25kN, the displacement should be 0.017mm, which corresponds with the numerical results.

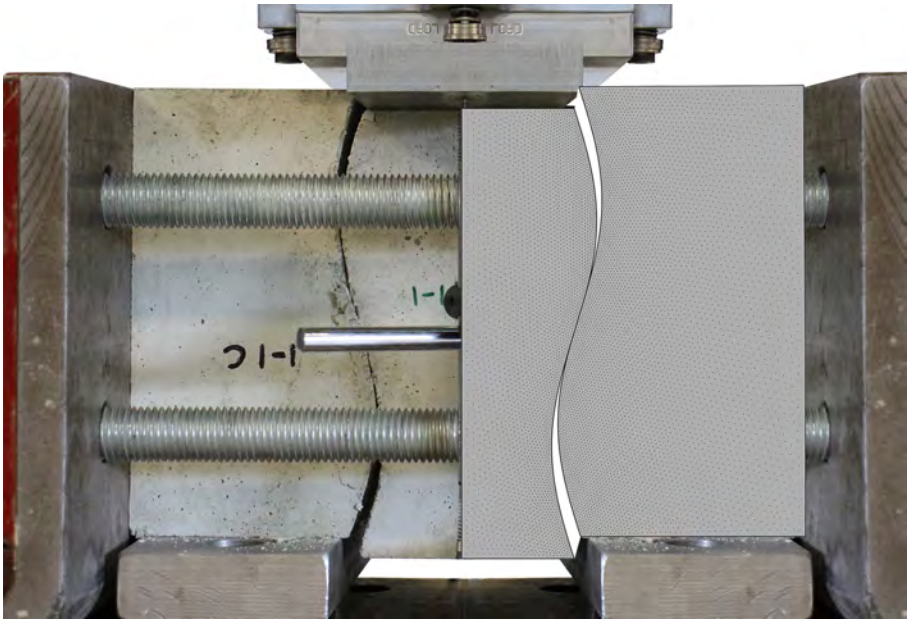

Figure 6.1: Displacements visible during the experimental (left) and numerical (right) analysis. Note that the deformations of the numerical results are scaled with a factor of 10.

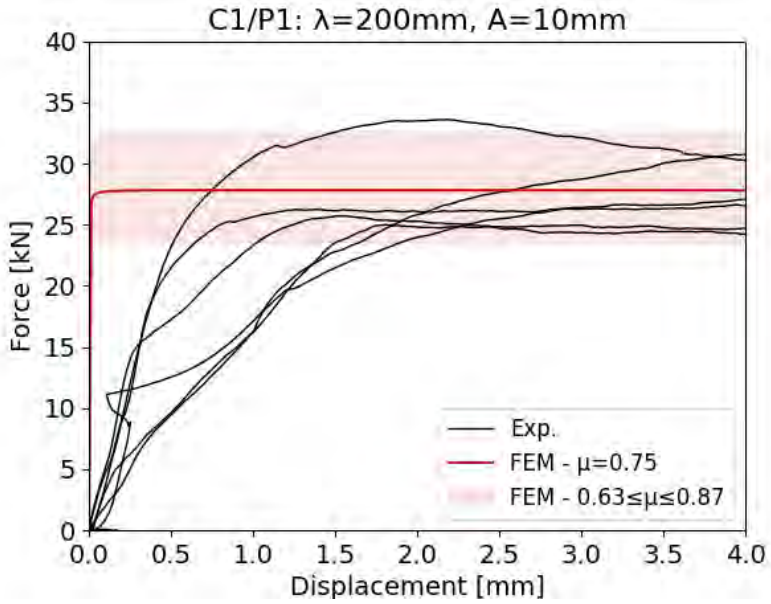

Figure 6.2: Load displacement response of the geometry C1 and P1. The experimental responses are shown in black, the numerical response for a friction coefficient of 0.75 is shown in red, and a red hatched area indicates a numerical spread corresponding to friction coefficients varying between 0.63 and 0.87.

Table 6.1 presents the slip-out force of five different tests performed in the experimental analysis. The slip-out forces in the experimental and numerical analysis are presented in this table. Furthermore, the force according to equation 5.6 is shown in the last column. Within equation 5.6 and for the numerical analysis, a friction coefficient of 0.75 was used. It can be seen that all three analyses give similar results. Therefore, if the friction coefficient is known and it is known that the connection will fail due to sliding, equation 5.6 can be used as a simple design tool.

Table 6.1: Slip-out force determined with the experimental analysis, numerical analysis and equation 5.6. A friction coefficient of 0.75 was used.

Geometry	Prestress [kN]	Experimental [kN]	Numerical [kN]	Eq. 5.6 [kN]
C1/P1	10	29.43	27.6	27.84
C1/P1	20	53.51	54.6	55.69
C2	10	67.68	51.6	52.13
P2	10	18.26	19.3	19.34
P2	20	32.24	38.4	38.67

6.2 Fracture

As explained in section 5.2.2, two different fracture mechanisms were found in the finite element analysis, one being mode I dominated (C4) and one being mode II dominated (C3). The two fracture patterns are compared to the experimental fracture patterns for the corresponding geometries. In figure 6.3, the fracture pattern of geometry C3 just after the peak force is visualised, as indicated in the force-displacement diagram in figure 6.7a. It can be seen that the crack pattern is not exactly the same, but in both cases, multiple cracks occur simultaneously within the notches of the sinusoid shape. When looking at the load-displacement response of the numerical and experimental analysis, as presented in figure 6.7a, the result of the simultaneously occurring cracks can be seen by a sudden drop of the shear force. Similar to the geometries which fail due to sliding, a significant difference in stiffness can be seen in the load-displacement responses of the numerical and experimental results. This can again be explained by 1 to 2 mm deviations within the interface surface. Furthermore, the strong force increase within the experimental response only starts at a vertical displacement of 0.5mm. These first settlements were caused by the different parts finding the optimal fit within the sinusoid connection, which can differ between the specimens due to different deviations within the interface.

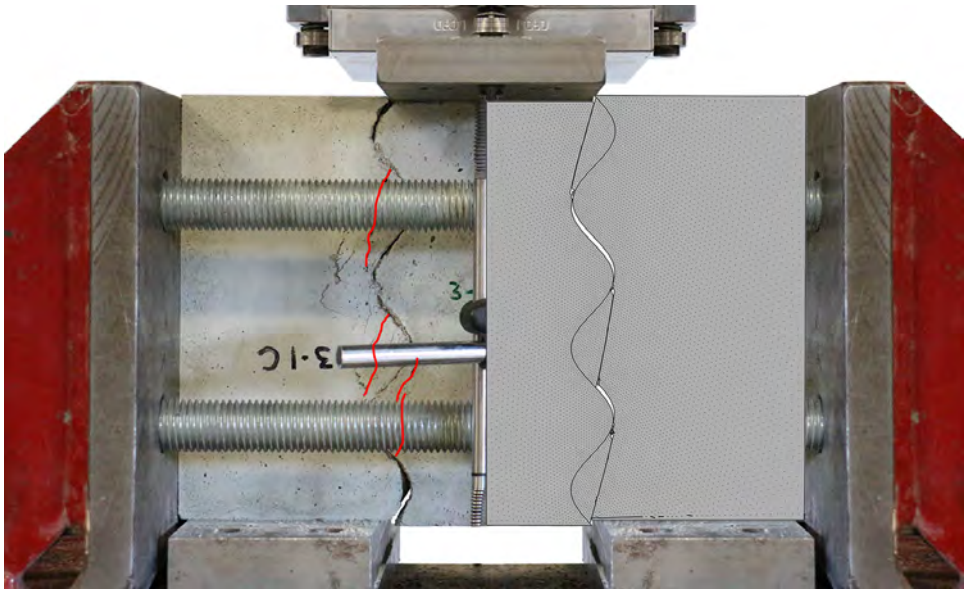

Figure 6.3: Displacements visible during the experimental (left) and numerical (right) analysis of specimen C3-1 just after the peak. Note that the deformations of the numerical results are scaled with a factor of 10.

Figures 6.5 and 6.6 show the fracture pattern of the experimental and numerical analysis of geometry C4 at the first and second drop within the force-displacement response, as indicated in figure 6.7b. In both the numerical and experimental results, the first drop of the applied vertical force is caused by a single crack. During the experimental tests, the first crack occurred in the second notch of the middle specimen, while in the numerical analysis, the crack occurred at the lowest notch. However, when looking at the maximum principle stresses of the numerical analysis, visible in figure 6.4, high tensile stresses occur at all three notches. Therefore, the exact location of the first crack can be highly dependent on the local strength properties within the specimens and the finite element discretisation.

When deformation increases, more cracks occur, as shown in figure 6.6. The overall crack pattern of the numerical and experimental results is similar, although not all cracks are in the same location. One significant difference within the crack patterns is the large crack on the right within the numerical results. This crack is not visible within the experimental results due to differences in the boundary conditions. The vertical support of the experimental test set-up can only transfer compression forces, while the support modelled in the numerical analysis can also transfer tensile forces. Due to the small lever arm within the notches of the sinusoid shape, the specimens want to rotate slightly. Within the experimental set-up, this is prevented by the steel plate on the left, which has to stay straight. In the numerical model, this rotation is prevented by the vertical support, leading to tensile stresses which caused the horizontal crack, these stresses are visible in figure 6.4 on the left side. A large drop of the vertical force is visible within the force-displacement response of the numerical analysis, visible in figure 6.7b. In contrast, this drop is significantly smaller for the experimental results. This horizontal crack could cause this difference.

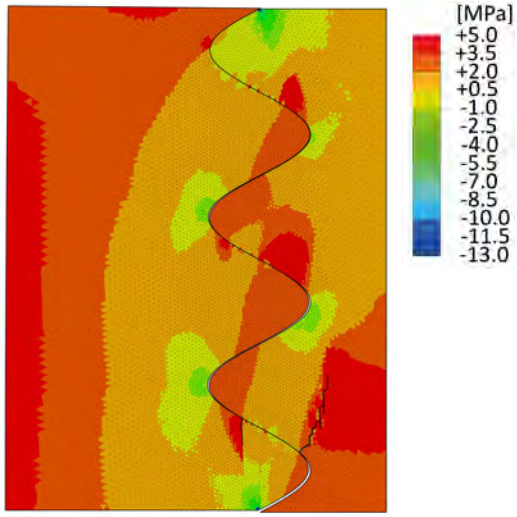

Figure 6.4: Maximum principle stresses in geometry C4 just after the first drop of the vertical force. Note that the deformations of the numerical results are scaled with a factor of 10.

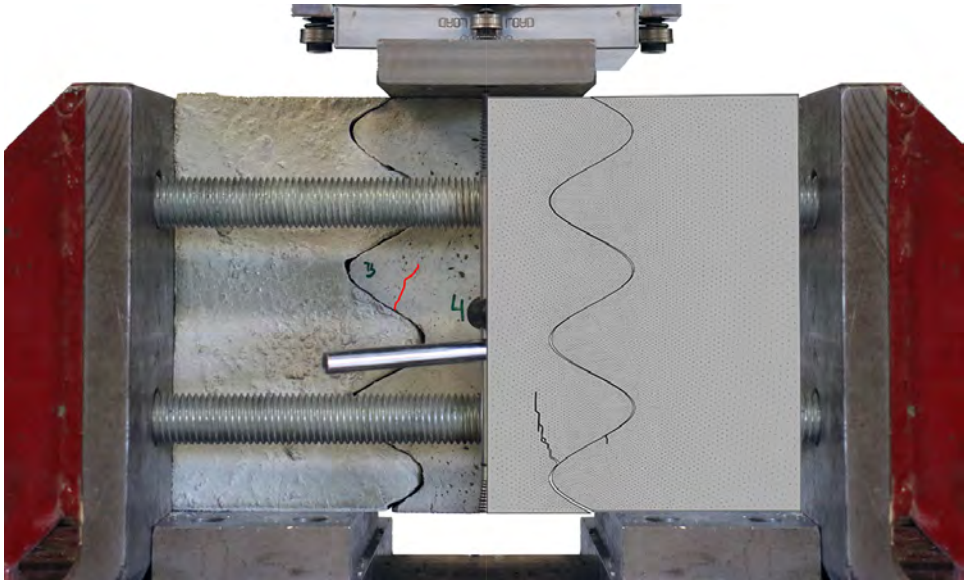

Figure 6.5: Displacements visible during the experimental (left) and numerical (right) analysis of specimen C4-1 just after the first drop of the vertical force. Note that the deformations of the numerical results are scaled with a factor of 10.

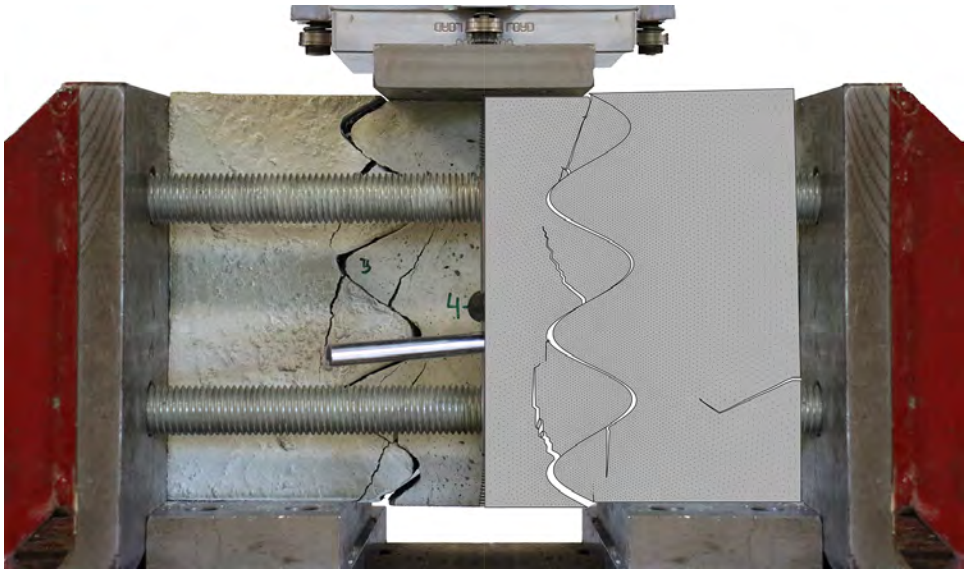

Figure 6.6: Displacements visible during the experimental (left) and numerical (right) analysis of specimen C4-1 just after the second drop of the vertical force. Note that the deformations of the numerical results are scaled with a factor of 10.

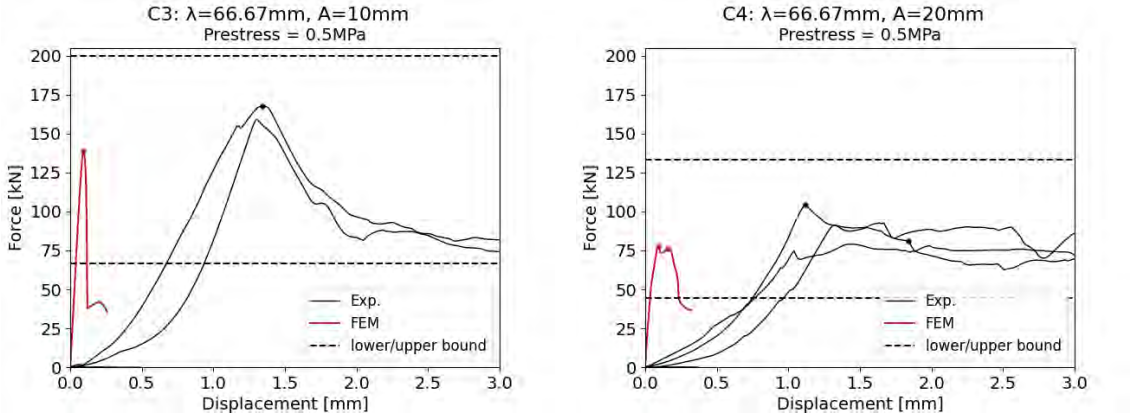

(a) **(b)**

Figure 6.7: Load displacement response of the geometries C3 (a) and C4 (b). The experimental responses are shown in black, and the numerical response is presented in red. The dashed lines represents the lower and upper bound as determined with equation 6.2 for geometry C3 and equation 6.1 for geometry C4.

Although the stiffnesses and the post-peak behaviour within the load-displacement responses given in figure 6.7 differ slightly, the behaviour at the peak is similar, where for geometry C3 the vertical force drops suddenly, and for C4 this drop is more step-wise. Similar values were found when looking at the magnitude of the ultimate force, presented in table 6.2. The table presents the ultimate shear force found in the experimental and numerical analyses for geometries C3, C4, C5 and C6, being two geometries loaded with two different applied prestresses. The ultimate forces found during the numerical analysis differ only by about 15% compared to the experimental results, with the exception of C6. This difference is 40%, which is still not significant, knowing that the differences within the experimental results of C6 were about 30%

When analysing the connection with a strut-and-tie model, the upper and lower bound of a mode I failure mechanism could be determined according to equation 5.10. As explained before, geometry C3 failed due to a mode II dominated behaviour, meaning the ultimate force cannot be determined by calculating the bending stress. For geometry C4, the lower and upper bound can be determined by solving equation 5.10 for F, see equation 6.1.

$$F = \frac{x \cdot \frac{1}{12} \cdot b \cdot \lambda^3 \cdot \sigma_b}{\frac{1}{4} \cdot A \cdot \lambda} \tag{6.1}$$

As two interfaces were tested simultaneously in the experimental set-up, for geometry C4, having three notches per interface, the value x can vary between 2 and 6 loaded notches. For the bending strength σ_b a value of 2.5MPa (similar to the value used in the finite element analysis) plus the applied prestress of 0.5MPa is used. This gives a lower bound of 44kN and an upper bound of 133kN, both are indicated in figure 6.7b by a dotted line. It can be seen that indeed all numerical and experimental results are between the calculated upper and lower bound.

For a geometry that fails due to shear failure, the shear stress in a notch can be determined by $F/A = F/(b \cdot \lambda)$. It is assumed that the shear strength of the material equals 5MPa. Therefore, a lower and upper bound for geometry C3 could be determined by:

$$F = x \cdot b \cdot \lambda \cdot \tau \tag{6.2}$$

For geometry C3 this gives a lower bound of 66.7kN and an upper bound of 200kN, indicated with a dotted line in figure 6.7a. Also for this geometry it can be seen that the numerical and experimental results are between the two determined values. If the lower and upper bound were to be calculated with equation 6.1 instead of equation 6.2, they would be equal to 88kN and 266kN respectively, which

is higher than the values determined for mode II failure. Therefore, indeed a mode II dominated failure is to be expected.

When looking at table 6.2, it can be seen that both the experimental and the numerical analyses show a decrease in ultimate shear force with an increase in amplitude, which corresponds to the results of the strut-and-tie analysis presented in section 5.4. Furthermore, an increase in the ultimate shear force with an increase in prestress can be seen both in the numerical and experimental results. For geometry C3/C5, this increase is 14% and 6% within the experimental and numerical analyses, respectively. For geometry C4/C6, this is 78% and 29%. Although the percentages are not the same, both analyses present a larger increase of the ultimate shear force due to an increase in prestess for geometry C4/C6. This difference in increase can be explained by the mode mixity, where the mode mixity parameter β confirmed a mode II dominated behaviour for geometry C3/C5 and a mode I dominated behaviour for C4/C6 within the numerical analyses. For a mode I dominated failure, cracks occur due to tensile stresses running almost horizontally through the notches (splitting tensile stresses), as illustrated with the tie in figure 5.10 in the strut-and-tie analyses. When increasing the prestress, these tensile stresses are cancelled out. If the amplitude of the sinusoid shape is smaller (C3/C5), failure does not occur due to these splitting tensile stresses but due to shear stresses, resulting in a mode II dominated behaviour. According to EN 1992-1-1 [26], the design shear strength of unreinforced concrete (f_{cvd}) can be calculated with equation 6.3, where $f_{ctd,pl}$ equals the design tension strength of concrete and σ_{cp} the applied axial stress. This equation shows that the shear strength increases with an increasing prestress, but it is less significant than when the tensile stresses are cancelled out in mode I dominated behaviour. This implies that, although the cracks visible in the experimental results of C3/C5 and C4/C6 look similar, C3/C5 is mode II dominated, and C4/C6 is mode I dominated.

$$f_{cvd} = \sqrt{f_{ctd,pl}^2 + \sigma_{cp} f_{ctd,pl}} \tag{6.3}$$

Table 6.2: ultimate shear force determined with the experimental and numerical analysis.

Geometry	Prestress [MPa]	Experimental [kN]	Numerical [kN]
C3 (λ=67mm, A=10mm)	0.5	160.05	139.02
C4 (λ=67mm, A=20mm)	0.5	94.14	77.85
C5 (λ=67mm, A=10mm)	1.0	181.96	147.60
C6 (λ=67mm, A=20mm)	1.0	167.35	100.8

The ultimate shear forces found in this study are comparable with the strengths of keyed joints analysed by Bischof et al. [5]. In their research, the shear strength of several different keyed joints with a height of 200mm and a width of 120mm was determined. When adjusting for the difference in width compared to this research, the shear strengths of these dry joints varied between 58 kN and 150 kN per interface for an applied prestress of 2.0 MPa. In this research, two interfaces were tested simultaneously, meaning that the presented forces should be divided by 2 to compare them. When looking at specimens C5 and C6, tested with an applied prestress of 1.0 MPa, the shear strength varied between 73 kN and 93 kN per interface.

Chapter 7

Manufacturability

This chapter describes the robotic manufacturability of the sinusoid connection and the influence of varying different shape parameters on the ease of manufacturing. Section 4.2 described how the printed specimens were prepared for the experimental research. The layers were printed in the desired sinusoid shape, and the surface was milled to achieve a higher precision. It was stated that the nozzle was always oriented perpendicular to the print layer. This is required to prevent the nozzle from touching the fresh concrete due to its own thickness. Furthermore, by re-orientating the nozzle depending on the sinusoid shape, the layers are more precise.

Despite the precision achieved by re-orienting the nozzle, milling was done to improve the surface. Figure 7.1 shows the surface of a printed specimen directly after printing (a) and after the surface was milled (b). It can be seen that the printed surface is not flat over the width of the specimen. Within the print path, slightly more material is extruded in the middle compared to the sides. By milling the surface, these irregularities are removed. This results in a higher contact area between the connected parts. Figure 7.2 shows the primary, waviness and roughness profiles of a milled surface. The milling tool had a diameter of 10mm and went over the specimen in a zigzag pattern. These rows are visible in the waviness profile resulting in deviations of approximately 0.3mm. The average roughness parameter R_z for the milled specimens was 0.58mm. For a surface printed on plastic, R_z was equal to 0.37mm. This shows that the achieved precision is comparable to the cast specimens and that milling results in a slightly rougher surface compared to printing/casting on plastic.

(a) Surface after printing **(b)** surface after milling

Figure 7.1: Surface of a printed specimen directly after printing (a) and directly after milling (b)

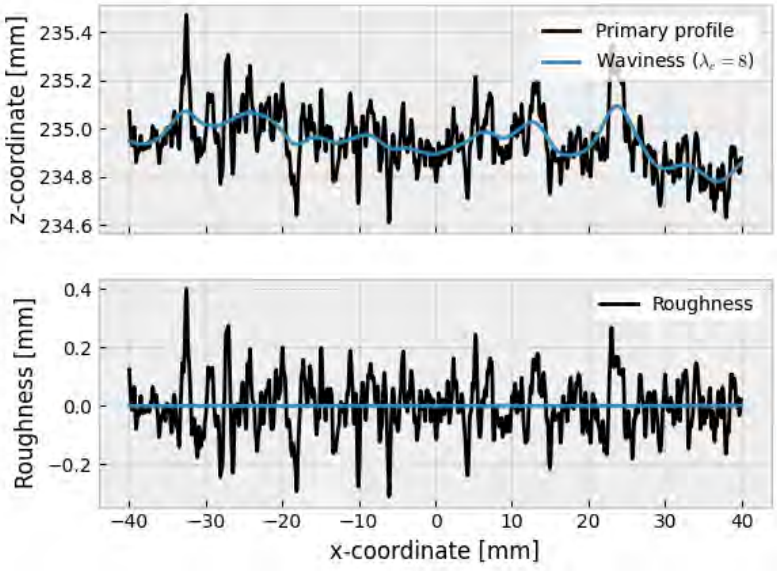

Figure 7.2: Primary, waviness and roughness profile of a milled surface

For this research, only specimens with a small maximum angle were printed. When larger angles were printed, the torsional force on the robotic arm was too high for this robot. Figure 7.3 illustrates the problem. Due to the sinusoid shape, the nozzle rotates, meaning that the hose connected to the nozzle rotates as well, as indicated in yellow. Due to the velocity of the hose during this rotation and its mass, a torsional force exists, which is counteracted by the robotic arm, as indicated in red. The faster this rotation has to be made, due to higher amplitudes or smaller wavelengths, the higher the torsional force.

Therefore, it can be concluded that sinusoid connections with smaller amplitudes or larger wavelengths are easier to manufacture. However, it does not mean that manufacturing larger amplitudes or smaller wavelengths is impossible. Within the set-up used in the laboratory of the Technical University of Eindhoven, the geometries were limited, but if the hose is connected to a gantry system at the top, this torsional force on the robotic arm could be prevented. Furthermore, larger amplitudes or smaller wavelengths could be achieved using a stronger robot. More extreme sinusoid shapes can thus be manufactured, but the set-up has more requirements.

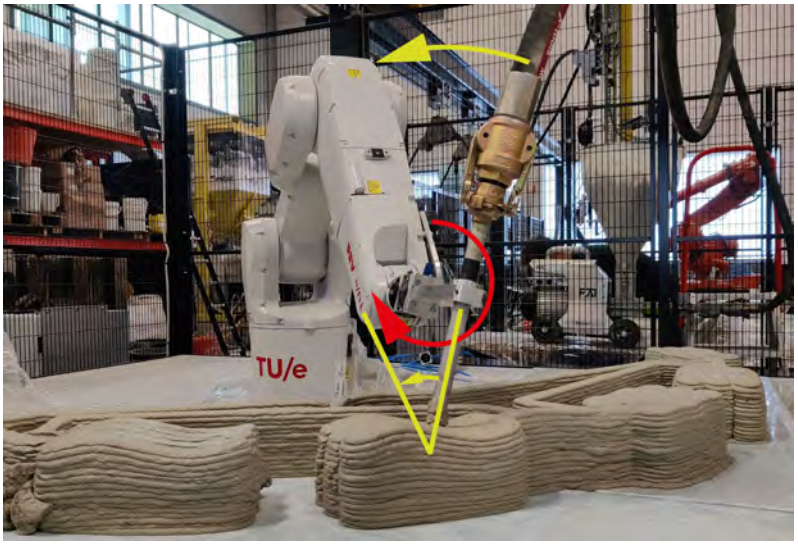

Figure 7.3: Torsional force on the robotic arm due to rotations of the nozzle

Chapter 8

Case Study

The findings of the experimental and numerical analyses were validated with a case study. The goal of the case study is to see how the connection behaves within a small structure and to see to what extent the findings can be used as design guidelines. As the connection is evaluated on the transfer of shear only, a shear wall is designed consisting of four parts connected with sinusoid connections. The structural behaviour of this structure is compared to a monolithic shear wall. This chapter presents the design concepts of the structure, the methodology of the experiments and the results in sections 8.1, 8.2 and 8.3, respectively.

8.1 Design

As mentioned, a shear wall consisting of four parts is compared to a monolithic variant. As the connection is evaluated for shear only, the wall is designed to fail due to shear forces. To prevent the necessity for an extremely high prestress to counteract the bending stresses, a wall with a width of 400mm and a height of 300mm was designed. The depth of the wall equals 100mm. On the structure, two horizontal shear forces are applied as visualised in figure 8.1. For the design, it is assumed that the shear strength of concrete is equal to 5.0 MPa, similar to the ultimate traction in mode II used in the numerical analysis. The smallest flexural strength measured during the 3-point bending tests had a value of 3.6 MPa. With a prestressing force of 40kN, resulting in a prestress (σ_{cp}) of 1.0 MPa, the maximum shear stress and bending stress can be determined with equations 8.1 and 8.2 respectively. To reach a shear stress of 5.0 MPa, V_{Ed} equals 135kN.

$$\tau = 1.5 \cdot \frac{V_{Ed}}{b \cdot d} = 5.06 \text{ MPa} \tag{8.1}$$

$$\sigma_b = \frac{My}{I} - \sigma_{cp} = 1.09 \text{ MPa} \tag{8.2}$$

Therefore, the first two connections, as indicated in figure 8.1, should be able to transfer 67.5kN and the third connection has to transfer 135kN. As the force on the first two connections is not extremely high, a connection that fails due to sliding is designed using equation 5.6. To be conservative, a friction coefficient of 0.65 is used, resulting in a required angle of 27 degrees, as can be seen in equation 8.3. This angle is achieved by a sinusoid shape with an amplitude of 8mm and a wavelength of 100mm.

$$F_{slip} = \frac{P \cdot \mu \cdot cos(\alpha) + P \cdot sin(\alpha)}{cos(\alpha) - \mu \cdot sin(\alpha)} = \frac{40 \cdot 0.65 \cdot cos(27) + 40 \cdot sin(27)}{cos(27) - 0.65 \cdot sin(27)} = 69.3 \text{ kN} \tag{8.3}$$

The force on the third connection is significantly higher. According to equation 5.6 an angle of 41 degrees is required for this force. The results of the previous analyses show that geometries with this angle will fail due to fracture instead of sliding, thus, a connection that fails due to sliding will not be able to transfer a force of 135kN. Therefore, a connection that fails due to fracture is designed. As the

different parts of the wall have a height of only 75mm, the amplitude cannot be large. Furthermore, the prestress is only 1.0 MPa, making it more beneficial to design a connection that fails due to mode II dominated behaviour. This can be achieved by designing a connection with a small amplitude and a small wavelength. By the small wavelength, the angle is large enough to prevent sliding and a small amplitude reduces the splitting tensile forces. Therefore, a mode II failure mechanism is expected. For these reasons, a connection with an amplitude of 10mm and a wavelength of 66.67mm is designed. Depending on whether the shear force is divided over all notches or only one, the shear stress within the notch will vary between 3.37 and 20.25 MPa for a force of 135kN.

$$\tau_1 = \frac{F}{\lambda \cdot d \cdot b/\lambda} = \frac{135000}{66.67 \cdot 100 \cdot 400/66.67} = 3.37 \text{ MPa} \tag{8.4}$$

$$\tau_2 = \frac{F}{\lambda \cdot d} = \frac{135000}{66.67 \cdot 100} = 20.25 \text{ MPa} \tag{8.5}$$

In the experimental and numerical analyses, multiple cracks occurred simultaneously, indicating that multiple notches were activated. Therefore, a shear stress of 20.25 MPa is unlikely and the stress will most likely be closer to 3.37 MPa, meaning that the connection should be able to transfer a force of 135kN.

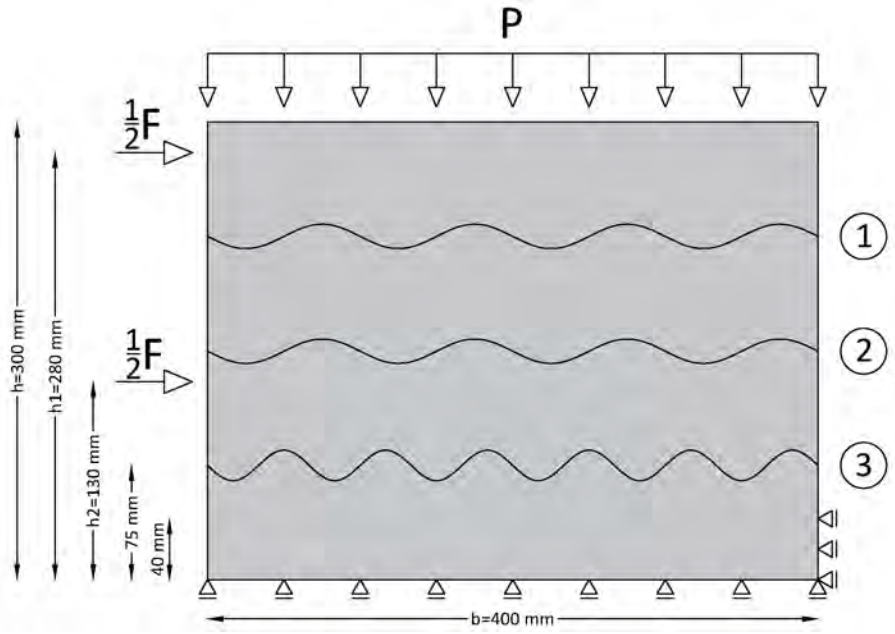

Figure 8.1: Design of a shear wall consisting of four parts connected by sinusoid connections

8.2 Methodology

For the case study, cast specimens were used. Three assembled walls, constructed of four parts each, and three monolithic walls were constructed. The formwork was created similar to the formwork used in the preliminary study explained in section 3.2.1. The concrete was mixed and cast as was done in the experimental analysis explained in section 4.2. The concrete was mixed in three batches, and for each batch, three mortar beams were cast to verify possible material deviations. After casting, the specimens were covered with plastic, and after 24 hours, the formwork was removed, and the specimens were placed underwater.

After seven days, the specimens were subjected to a shear test. The shear capacities of the assembled and monolithic walls were determined using the test set-up illustrated in figure 8.2. The set-up

is similar to the previous studies, which is explained in more detail in section 3.3.1. During the experiments, the vertical displacements at the top of parts A, B and C, as indicated in figure 8.2, were measured at the front and back of the wall. Furthermore, the applied force and applied prestressing force were measured. The dimensions of the specimens and the plates used as support and loading conditions are indicated in figure 8.2.

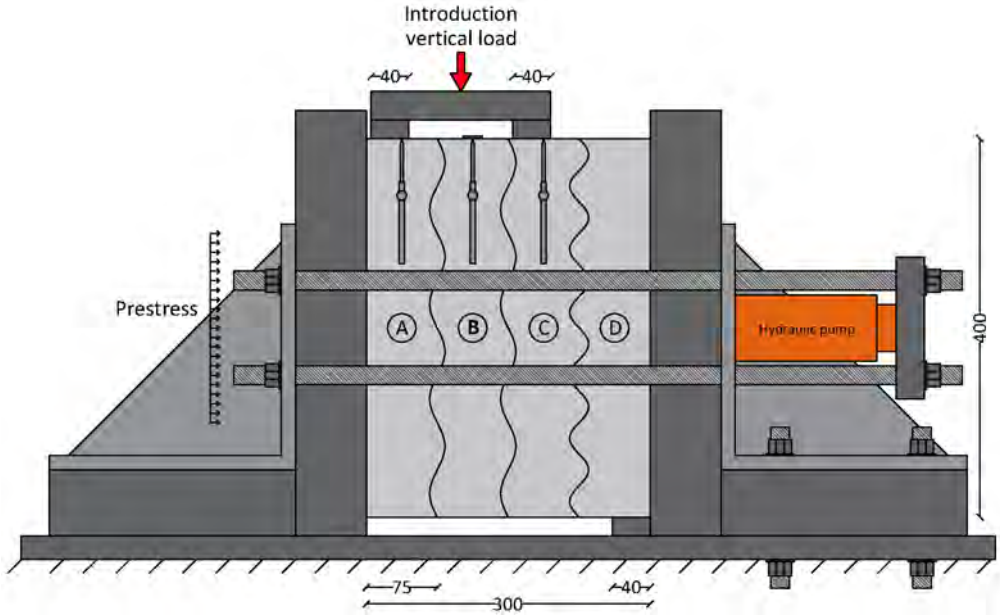

Figure 8.2: Test set-up for the shear test on a small scale shear wall. The displacements were measured at the top of the specimens relative to the absolute world, and the dimensions are given in millimetres.

8.3 Results

Table 8.1 presents the results of the 3-point bending test and the uni-axial compression test for the three different batches used. The flexural strengths are comparable to the results presented in section 4.3. The compressive strengths are slightly lower, possibly due to a shorter hardening time. The deviations in material strength between the three batches are not significant. The relative standard deviation for the flexural strength equals 3.67%, and for the compressive strength, this equals 1.74%, both smaller than the deviations within the different batches.

Table 8.1: Flexural strength and compressive strength of the three different batches of concrete used for the monolithic wall (batch 1 and 2) and the wall including connections (batch 2 and 3)

Concrete batch	Flexural strength [MPa]	Relative stdv. [%]	Compressive strength [MPa]	Relative stdv. [%]
1	5.66	1.51	33.32	2.95
2	5.72	4.41	32.13	2.25
3	5.26	7.42	33.36	6.54

The results of the shear tests on a small scale shear wall are presented in figure 8.3, figure 8.4 and table 8.2. Figure 8.3 shows the failure mechanism of an assembled wall. All three structures failed due to fracture of the most right connection. This connection also has to transfer the highest force. The load-displacement response is presented in figure 8.4 where the vertical force is plotted against the displacement of part C. The upwards displacement due to the application of the prestressing force

is not included in the force-displacement responses but did differ for the monolithic and assembled walls. The monolithic walls had an average upwards displacement of 0.08mm compared to a displacement of 0.86mm for the assembled walls. The displacements of parts A and B were measured as well. Similar results were found, although the deformations were slightly higher due to a rotation of the complete wall. These force-displacement responses are visible in appendix B. Figure 8.4 shows a difference in deformation capacity between the assembled and monolithic walls. The monolithic wall fails at a displacement of around 1.75mm, whereas the assembled wall only fails at 2.65mm. Despite these differences, the load-displacement responses of the assembled and monolithic walls show similar behaviour of a strong increase of force, after which the force reduces.

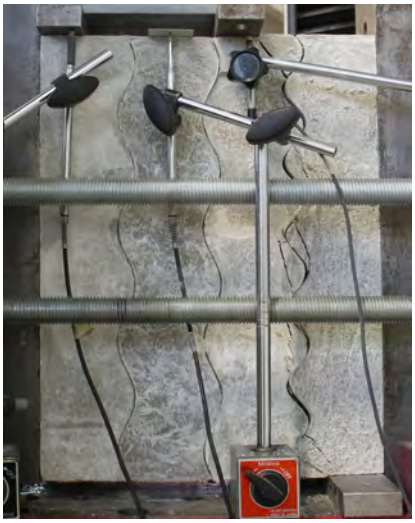

Figure 8.3: Failure mechanism of the wall assembled from 4 parts.

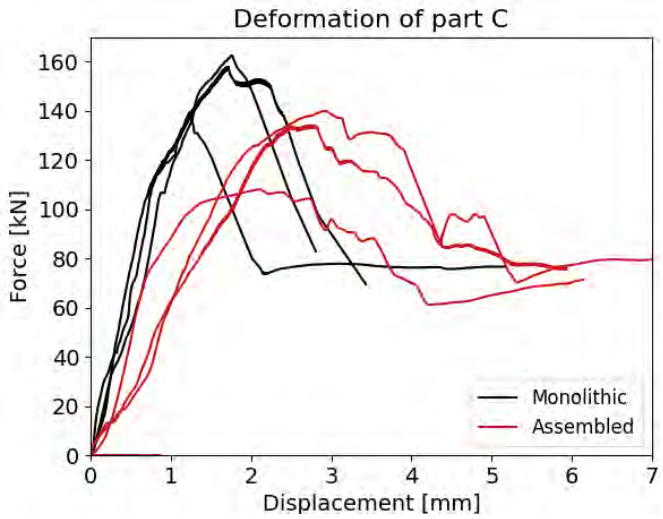

Figure 8.4: Load-displacement responses of the monolithic (black) and assembled walls (red). The displacement represents the vertical displacement of part C.

Within table 8.2, the ultimate shear forces of the assembled and monolithic walls are presented. Furthermore, an extra test of a wall being assembled with only the weaker connection (λ=100mm, A=8mm) is included. The results show that the assembled wall has a shear capacity of 83.12% compared to a monolithic wall. The wall was designed for a shear load of 135kN, as explained in section 8.1. The ultimate shear forces found in the shear tests are close to this design value, with a maximum reduction of 20% for the assembled walls and a maximum increase of 20% for the monolithic walls. The extra test performed with an assembled wall with only the weaker connection resulted in an ultimate shear force of 90kN. This is slightly higher than the calculated value of 69.35kN according to equation 5.6, which is most likely due to a higher friction coefficient. A friction coefficient of 0.81 would lead to an ultimate shear force of 90kN. This wall failed due to sliding as expected. At a displacement of 4.5mm, a crack started to occur, but sliding failure already started at a displacement of 1mm. The force-displacement response of this test is included in appendix B as well.

Table 8.2: Ultimate shear forces on the shear wall consisting of four elements (assembled wall) and on the monolithic wall. An extra test being an assembled wall with only the weaker connection, is included in the last row.

	Test 1 [kN]	**Test 2 [kN]**	**Test 3 [kN]**	**Average [kN]**	**Failure mechanism**
Assembled wall	140.02	108.23	134.07	**127.44**	fracture
Monolithic wall	139.51	162.26	157.88	**153.32**	fracture
Extra test	90.03			**90.03**	sliding

Chapter 9

Conclusions and recommendations

9.1 Conclusions

This research aimed to establish design recommendations for demountable connections in prefabricated 3D concrete printed elements based on the varying shear capacity of the connection. During a preliminary study, where different geometries were analysed, it was concluded that based on a combination of manufacturability, structural behaviour and adaptability, a sinusoid geometry had the most potential. Therefore, a more detailed analysis was performed on a sinusoid connection. The main conclusions of the potentials of a sinusoid connection, the influence of certain design choices on the mechanical behaviour and the influence of these choices on the manufacturability will be presented separately in sections 9.1.1, 9.1.2 and 9.1.3 respectively. Lastly, section 9.1.4 summarises the design recommendations based on the results of this research.

9.1.1 Assessment of the potential of a sinusoid connection

In section 2.1, three requirements of a connection were presented: (i) The connection should be able to transfer all forces, (ii) it should not restrict deformations of the structure itself, and (iii) a ductile failure mechanism is preferable. During the case study, it was shown that the tested wall consisting of four parts connected with a sinusoid connection has a shear capacity of 83.12% and a higher deformation capacity compared to a monolithic wall. Therefore, it can be concluded that the first two requirements could be met depending on the forces within the to-be-assembled structure. Although ductility is not a requirement but a preference, this box cannot be checked thoroughly. The geometries that fail due to sliding show some form of ductility, but even in those cases, the shear force does not increase after the linear part. However, the lack of ductility may be solved by adding reinforcement.

Besides the mechanical requirements, a connection should be manufacturable. The sinusoid connection was manufactured digitally during the experimental analysis, proving the possibility of digital manufacturing. The connection uses simple geometrical interlocking principles without the use of sophisticated, high-performance materials, which results in less elaborate joining processes, as mentioned in section 2.1. Therefore, despite the lack of ductility, it can be concluded that based on the mechanical behaviour and the manufacturability, the sinusoid connection shows a lot of potentials. However, accidental disassembly, one of the problems of mechanical joining as mentioned in section 2.1, may cause problems and need further research.

9.1.2 Influence of certain design choices on the mechanical behaviour

A more detailed analysis of a sinusoid connection showed two different failure mechanisms. Dependent on the roughness of the interface surface, the strength of the concrete, the applied prestress, and the maximum angle of the sinusoid shape, a sinusoid connection fails due to sliding or fracture.

Sliding along the sinusoid interface

The force-displacement response of this failure mechanism shows a bi-linear relationship, where the first part represents the force increase, after which a horizontal plateau is reached. It was found that the slip-out force can be determined with equation 5.6. According to this equation, the slip-out force increases when the angle increases, the friction coefficient is larger, or when the applied prestress is higher.

If there are significant deviations within the interface surface or if the roughness is high, a peak can be seen within the force-displacement response. The shear force first decreases, after which the horizontal plateau is reached.

Fracture

Two types of fractures can occur. If the amplitude is large, the lever arm leads to high splitting tensile stresses, resulting in a mode I dominated failure. When the amplitude is smaller, the splitting tensile stresses are smaller, and fracture can occur due to the shear stresses, leading to a mode II dominated failure.

The results showed that a larger amplitude leads to a smaller ultimate shear force, as can be validated with a strut-and-tie model. This is also valid if the failure mechanism changes from mode II dominated to mode I dominated, as the shear strength of concrete is higher than the tension strength. Furthermore, the strut-and-tie analysis showed that the ultimate shear force decreases if the wavelength decreases, although the exact nature of this relationship is unknown because the distribution of forces over the different notches is unknown. Lastly, the results showed a positive effect of an increase in prestress on the ultimate shear force. The increase of the ultimate shear force was higher for geometries that showed mode II dominated failure.

9.1.3 Influence of certain design choices on the manufacturability

Within the robotic set-up used at the Technical University of Eindhoven, only small amplitudes and large wavelengths were possible to manufacture. With a more evolved set-up, other geometries should be possible to manufacture as well. Thus, to manufacture more extreme shapes, the robotic set-up needs to fulfil more requirements.

9.1.4 Design recommendations

If the required shear capacity is small, it is recommended to use a small maximum angle to design a connection that fails due to sliding, as this failure mechanism has a large deformation capacity and designing a smaller angle could simplify the manufacturing process. The connection can then be designed according to equation 5.6, and the shear capacity can be increased by increasing the maximum angle, the prestressing force or the friction coefficient.

If a high shear capacity is required, a connection which fails due to fracture should be designed, as high shear forces cannot be achieved without a fracture failure mechanism. Depending on the amount of prestress, a connection with a mode I (large amplitude) or mode II (small wavelength) failure mechanism can be designed. If the prestress is relatively small, a mode II failure mechanism is recommended, as the shear strength of concrete is higher than the tensile strength. For a high applied prestress a mode I dominated failure mechanism could be beneficial as the splitting tensile stresses are mostly counteracted by the prestress. A Finite Element Analysis, including cohesive zone modelling, could give an indication of the shear capacity of these connections. Still, more research is required for a direct derivation of the capacity.

9.2 Recommendations for further research

To make it possible to use this type of connection in practice, further research on the sinusoid connection is required. First of all, the risk of accidental disassembly should be assessed, and if required, a solution for this problem should be designed. As mentioned in section 2.1, for mechanical joining techniques extreme loading conditions can result in accidental disassembly, which can lead to a chain collapse of the whole structure. The risk of this phenomena should therefore be assessed and some adjustments or requirements for the design might be necessary. For most snap-fit connections, complex sequential motions are used to prevent sudden disassembly [21], which is not the case for the sinusoid connection. However, if the post-tensioning tendons are secured carefully and the amplitude of the sinusoid shape is not too small, the sinusoid geometries should have no space to disassemble. Research should be carried out to verify this assumption.

Furthermore, the behaviour of the geometries which fail due to fracture should be studied more extensively in order to be able to make an accurate prediction of the ultimate shear force. With the results of those studies, a tested calculation method could be developed. Lastly, the effect of scale should be analysed. This research focused on small-scale specimens and a small-scale structure. Increasing the scale could result in valuable information about the performance of the connection in larger structures.

The mechanical behaviour and manufacturing process of the connection could be further optimised. The mechanical behaviour could be optimised by studying (i) the influence of adding an interlayer of certain materials between the two to be connected parts, (ii) the influence of adding reinforcement and (iii) the capacity of the connection in relation to other types of forces (e.g., shear in the other direction, cyclic loading and bending). The results of the preliminary study with regards to adding an interlayer, presented in section 3.3.2, showed a decrease in force and higher deformations. However, the addition of an interlayer was not tested for a sinusoid shape, and previous research performed by Yu [33] did show an increase in the shear force due to the addition of certain interlayers. Adding reinforcement could also significantly increase the shear capacity of the geometries that fail due to fracture. Furthermore, similar to traditional reinforced concrete, yielding of the reinforcement can prevent sudden fracture and function as a warning system. Lastly, to be able to use the connection in practice, the effect of other types of loading conditions should be analysed to know in which kind of structures the connection could be applied. for example, to apply the connection in a bridge structure, the behaviour related to cyclic loading should be known.

From a manufacturing point of view, the set-up and the process itself could be optimised. As explained, the robotic set-up used for this research was insufficient, and a more extensive set-up should be designed. Besides the set-up itself, more research could be carried out on how the connection is manufactured. Within this research, the connection was manufactured based on the research performed by Ferguson [12]. Within his work, the optimal way of manufacturing is not analysed to a high extent. Analysing this could increase the precision, increase the possibilities and decrease the costs (both environmentally and financially) of manufacturing.

References

[1] Z. Y. Ahmed et al. “On-demand additive manufacturing of functionally graded concrete”. In: *Virtual and Physical Prototyping* 15.2 (Apr. 2020), pp. 194–210. ISSN: 17452767. DOI: 10.1080/17452759.2019.1709009. URL: https://www.tandfonline.com/action/journalInformation?journalCode=nvpp20.

[2] A. Baghdadi et al. “Experimental and numerical assessment of new precast concrete connections under bending loads”. In: *Engineering Structures* 212 (June 2020). ISSN: 18737323. DOI: 10.1016/J.ENGSTRUCT.2020.110456.

[3] A. Baghdadi et al. “Experimental and Numerical Assessments of New Concrete Dry Connections concerning Potentials of the Robotic Subtractive Manufacturing Technique”. In: *Buildings* 13 (Jan. 2023). ISSN: 20755309. DOI: 10.3390/buildings13010210.

[4] G. L. F. Benachio, M. C. D. Freitas, and S. F. Tavares. *Circular economy in the construction industry: A systematic literature review*. July 2020. DOI: 10.1016/j.jclepro.2020.121046.

[5] P. Bischof et al. “Experimental exploration of digitally fabricated connections for structural concrete”. In: *Engineering Structures* 285 (June 2023), p. 115994. ISSN: 0141-0296. DOI: 10.1016/J.ENGSTRUCT.2023.115994.

[6] M. V. Cid Alfaro, A. S.J. Suiker, and R. De Borst. “Transverse failure behavior of fiber-epoxy systems”. In: *Journal of Composite Materials* 44.12 (June 2010), pp. 1493–1516. ISSN: 00219983. DOI: 10.1177/0021998309360941.

[7] M. V. Cid Alfaro et al. “Analysis of fracture and delamination in laminates using 3D numerical modelling”. In: *Engineering Fracture Mechanics* 76.6 (Apr. 2009), pp. 761–780. ISSN: 00137944. DOI: 10.1016/j.engfracmech.2008.09.002.

[8] J. Dobrzanski et al. “Milling a cement-based 3D printable mortar in its green state using a ball-nosed cutter”. In: *Cement and Concrete Composites* 125 (Jan. 2022). ISSN: 09589465. DOI: 10.1016/j.cemconcomp.2021.104266.

[9] Ellen MacArthur Foundation. *Towards a circular economy: Business rationale for an accelerated transition*. Tech. rep. Nov. 2015.

[10] K. S. Elliott. *Precast Concrete Structures*. Butterworth-Heinemann, 2002. ISBN: 0 7506 5084 2.

[11] FEBE. *Les 4-Constructieve verbindingen 4.1 Algemeen*. Tech. rep. 2013. URL: https://febe.be/nl/publicaties/detail/modelcursus-prefab-beton?utm_source=febe&utm_medium=fork-search&utm_term=constructieve+verbinding.

[12] M. Ferguson. *A Digital Workflow for the Design and Manufacturing of 3D Printed Concrete Bridges in a Circular Economy: A Parametric Approach to Integrated Design and Fabrication*. Tech. rep. 2022.

[13] L. Hass, F. P. Bos, and T. A. M. Salet. “Characterizing the bond properties of automatically placed helical reinforcement in 3D printed concrete”. In: *Construction and Building Materials* 355 (Nov. 2022), p. 129228. ISSN: 09500618. DOI: 10.1016/j.conbuildmat.2022.129228. URL: https://linkinghub.elsevier.com/retrieve/pii/S0950061822028847.

[14] H. Kloft et al. “Additive Fertigung im Bauwesen: erste 3-D-gedruckte und bewehrte Betonbauteile im Shotcrete-3-D-Printing-Verfahren (SC3DP)”. In: *Bautechnik* 96.12 (Dec. 2019), pp. 929–938. ISSN: 14370999. DOI: 10.1002/bate.201900094.

[15] U. Knaack, S. Hickert, and L. Hildebrand. *Concretable*. Rotterdam: Nai010 Publishers, 2015. ISBN: 978-94-6208-221-2.

[16] J. Kunecký et al. “Experimental assessment of a full-scale lap scarf timber joint accompanied by a finite element analysis and digital image correlation”. In: *Construction and Building Materials* 76 (Feb. 2015), pp. 24–33. ISSN: 09500618. DOI: 10.1016/J.CONBUILDMAT.2014.11.034.

[17] R. Leach. “Surface topography characterisation”. In: *Fundamental Principles of Engineering Nanometrology*. Elsevier Science, Jan. 2014, pp. 241–294. ISBN: 9781455777532. DOI: 10.1016/B978-1-4557-7753-2.00008-6.

[18] S. Lehmberg et al. “Von der Bauteilfügung zu leichten Tragwerken: Trocken gefügte Flächenelemente aus UHPFRC”. In: *Beton- und Stahlbetonbau* 111.12 (Dec. 2016), pp. 806–815. ISSN: 14371006. DOI: 10.1002/best.201600053.

[19] L. Ma et al. “Effect of drying environment on mechanical properties, internal RH and pore structure of 3D printed concrete”. In: *Construction and Building Materials* 315 (Jan. 2022). ISSN: 09500618. DOI: 10.1016/j.conbuildmat.2021.125731.

[20] J. Mainka et al. “Non-Standard Fügeprinzipien für leichte Bauteile aus UHPFRC”. In: *Beton- und Stahlbetonbau* 108.11 (Nov. 2013), pp. 763–773. ISSN: 00059900. DOI: 10.1002/best.201300055.

[21] R. W. Messler. *Joining of Materials and Structures: From Pragmatic Process to Enabling Technology*. Elsevier, Jan. 2004, pp. 45–103. ISBN: 9780750677578. DOI: 10.1016/B978-0-7506-7757-8.X5000-3. URL: http://www.sciencedirect.com:5070/book/9780750677578/joining-of-materials-and-structures.

[22] M. E. Mohamad et al. “Friction and cohesion coefficients of composite concrete-to-concrete bond”. In: *Cement and Concrete Composites* 56 (Feb. 2015), pp. 1–14. ISSN: 0958-9465. DOI: 10.1016/J.CEMCONCOMP.2014.10.003.

[23] R. Mokhtar. *Behaviour of precast beam-to-column connections by using partly hidden corbel*. Tech. rep. University of Malaya, 2017.

[24] F. Moretti. *Concrete beam created with 3D printing*. Aug. 2015. URL: https://www.3dwasp.com/en/concrete-beam-created-with-3d-printing/.

[25] NEN. *NEN 1015-11 Methods of test for mortar for masonry - Part 11: Determination of flexural and compressive strength of hardened mortar*. Tech. rep. 1999.

[26] NEN. *NEN-EN 1992-1-1 Eurocode 2: Design of concrete structures - Part 1-1: General rules and rules for buildings*. Tech. rep. Apr. 2005.

[27] H. W. Reinhardt and S. Xu. “A practical testing approach to determine mode II fracture energy G I I F for concrete”. In: *International Journal of Fracture* 105 (2000), pp. 107–125.

[28] P. M. D. Santos, E. N. B. S. Júlio, and V. D. Silva. “Correlation between concrete-to-concrete bond strength and the roughness of the substrate surface”. In: *Construction and Building Materials* 21.8 (Aug. 2007), pp. 1688–1695. ISSN: 0950-0618. DOI: 10.1016/J.CONBUILDMAT.2006.05.044.

[29] P. Sharafi et al. “Interlocking system for enhancing the integrity of multi-storey modular buildings”. In: *Automation in Construction* 85 (Jan. 2018), pp. 263–272. ISSN: 09265805. DOI: 10.1016/J.AUTCON.2017.10.023.

[30] T. Sumiyoshi and G. Matsui. *Wood Joints in Classical Japanese Architecture*. 1991. URL: https://archive.org/details/wood-joints-in-classical-japanese-architecture/page/n3/mode/2up.

[31] A. Turon et al. “A damage model for the simulation of delamination in advanced composites under variable-mode loading”. In: *Mechanics of Materials* 38.11 (Nov. 2006), pp. 1072–1089. ISSN: 01676636. DOI: 10.1016/J.MECHMAT.2005.10.003.

[32] A. Turon et al. “Accurate simulation of delamination growth under mixed-mode loading using cohesive elements: Definition of interlaminar strengths and elastic stiffness”. In: *Composite Structures* 92.8 (July 2010), pp. 1857–1864. ISSN: 02638223. DOI: 10.1016/j.compstruct.2010.01.012.

[33] R. Yu. *A Digital Workflow for the Design and Manufacturing of 3D Printed Concrete Bridges in a Circular Economy: Structural Design Considerations for Pre-Stressed Beams and Dry Connections*. Tech. rep. 2022.

Appendix A

Results 4-point bending test for calibration mode I parameters

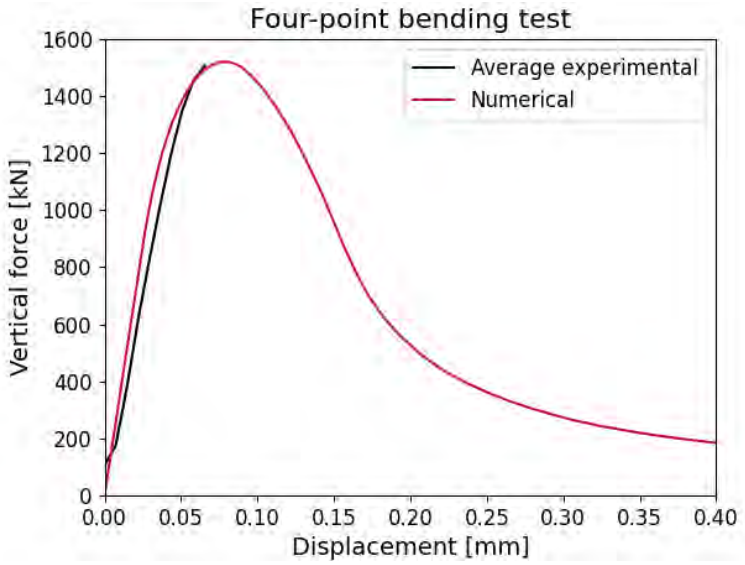

Figure A.1: Average load-displacement response of the experimental 4-point bending tests compared to the load-displacement response of the calibrated numerical model.

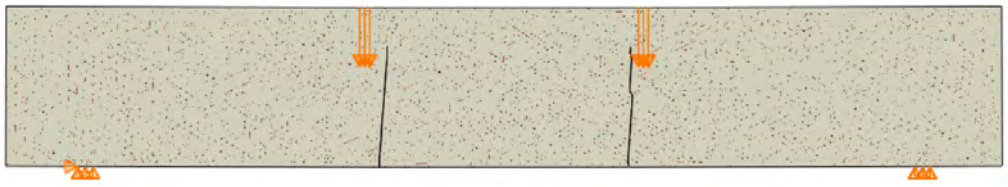

Figure A.2: Crack pattern of the numerical analysis of a 4-point bending tst

Appendix B

Results Case Study

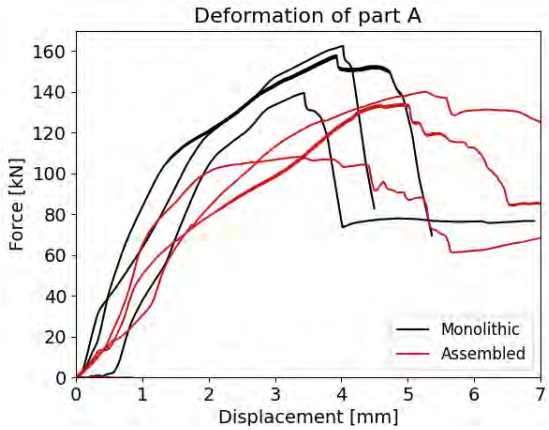

Figure B.1: Load-displacement responses of the monolithic (black) and assembled walls (red). The displacement represents the vertical displacement of part A.

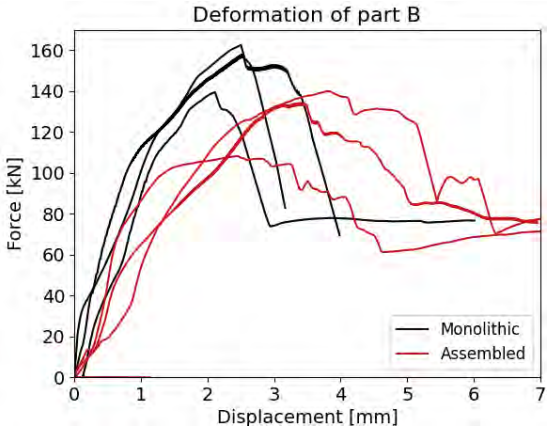

Figure B.2: Load-displacement responses of the monolithic (black) and assembled walls (red). The displacement represents the vertical displacement of part B.

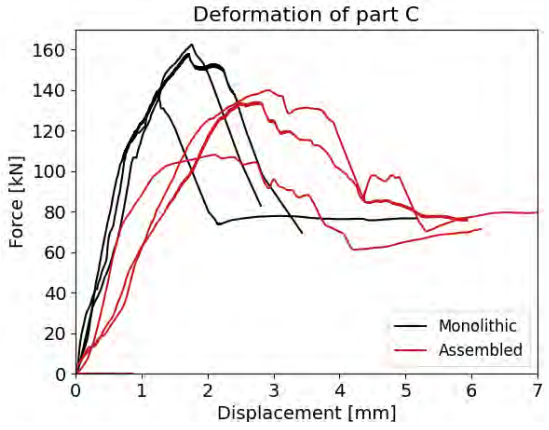

Figure B.3: Load-displacement responses of the monolithic (black) and assembled walls (red). The displacement represents the vertical displacement of part C.

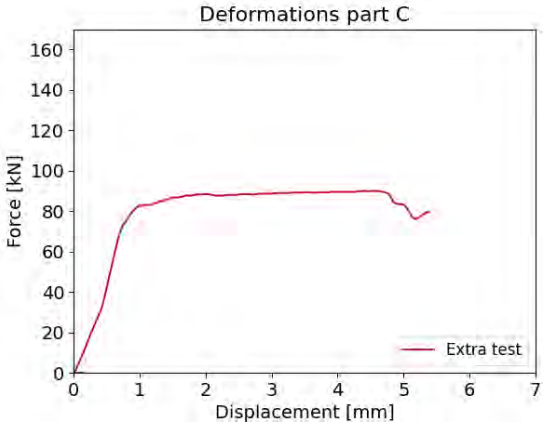

Figure B.4: Load-displacement responses of the extra test of an assembled wall connected by the weaker connection (λ=100mm, A=8mm). The displacement represents the vertical displacement of part C.